Fault flexure and lithospheric rheology set from climate cycles in the Corinth Rift

Gino de Gelder[1*], David Fernández-Blanco[1], Daniel Melnick[2,3], Guillaume Duclaux[4], Rebecca E. Bell[5], Julius Jara-Muñoz[2], Rolando Armijo[1] and Robin Lacassin[1]

1) Institut de Physique du Globe de Paris, Sorbonne Paris Cité, Université Paris Diderot, UMR 7154 CNRS, 1 Rue Jussieu, F-75005, Paris, France

2) Institut für Erd- und Umweltwissenschaften, Universität Potsdam, Karl-Liebknecht-Strasse 24, 14476 Potsdam, Germany

3) Instituto de Ciencias de la Tierra, Universidad Austral de Chile, Casilla 567, Valdivia, Chile

4) Université Côte d'Azur, UNS, CNRS, OCA, IRD, Géoazur, 06560 Valbonne, France

5) Basins Research Group (BRG), Department of Earth Science & Engineering, Imperial College, Prince Consort Road, London SW7 2BP, UK

*Corresponding author: gelder@ipgp.fr

Abstract

Geomorphic strain markers accumulating the effects of many earthquake cycles help to constrain the mechanical behaviour of continental rift systems as well as the related seismic hazards. In the Corinth Rift (Greece), the unique record of onshore and offshore markers of Pleistocene ~100-ka climate cycles provides an outstanding possibility to constrain rift mechanics over a large range of timescales. Here we use high-resolution topography to analyse the 3D geometry of a sequence of Pleistocene emerged marine terraces associated with flexural rift-flank uplift. The onshore dataset is integrated with offshore seismic data to provide a synoptic view of the flexural deformation across the rift. We find 4.5-9.0 mm·yr^{-1} of average slip

rate on the master fault over the past ~610 ka and an uplift/subsidence ratio of 1:1.2-2.4. To reproduce the observed flexure patterns, we use 3 and 5-layered lithospheric scale finite element models. Modelling results imply that the observed elastic flexure is produced by coseismic slip along 40-60° planar normal faults in the elastic upper crust, followed by postseismic viscous relaxation occurring within the basal lower crust or upper mantle. We suggest that such a mechanism may typify rapid localised extension of continental lithosphere.

Main text

Extension in continental rifts is characterised by normal faulting in the seismogenic upper crust, and a combination of brittle and/or ductile deformation in the underlying lower crust and upper mantle[1]. Our primary understanding of lithospheric extension mechanisms and rheological layering within such rifts is based on observations of the earthquake cycle at short timescales (10^0-10^3 yr)[2–5], or of evolved mature rift systems formed over geological timescales (10^6-10^8 yr)[6–9]. However, observations of deformation in modern active continental rifts - as documented by geology and geomorphology thus integrating many earthquake cycles - allows for incorporating crustal deformation at spatial scales of tens of km and on timescales of 10^4-10^6 yr. Here we aim to characterize lithospheric rheology and extension mechanisms at the young and very fast-evolving Corinth Rift in Greece (Fig. 1), an asymmetric rift born in the Pleistocene[10,11]. Along the southern rift shoulder, a 130-km-long north-dipping major fault system controls upward flexure associated with ~2-km of footwall uplift at rates of ~1.3 mm·yr^{-1} [10], counterbalanced by downwarped flexure associated with more than 3-km of hanging-wall subsidence[12]. Footwall flexural uplift has deformed a sequence of emerged Pleistocene marine terraces correlated with 100-ka climate cycles and dramatically modified the fluvial drainage network.

The global ~100-ka glacial-interglacial cycles correlate well with the most important variations of global temperatures and sea-level over the past 1200-800 ka[13,14]. In the Corinth Rift, sea-level variations have left their imprint on both sides of the main north-dipping fault

system. In the southern onshore domain, the superposition of glacio-eustatic sea-level variations on rapid flexural uplift resulted in an increasingly back tilted sequences of wave-cut marine terraces (Fig. 1). In the offshore domain, bathymetric sills[15,16] controlled sedimentation in the Gulf as a function of the same sea-level variations, switching rhythmically from lacustrine environment during sea-level lowstands to marine during highstands[17,18]. Taking advantage of this exceptional geological setting and combined geomorphic/stratigraphic record, we focus our high-resolution analysis on the uplifted marine terraces between the towns of Corinth and Xylokastro (Fig. 1). Here previous studies have revealed a systematic elevation decrease with distance from the main north-dipping fault system[10,19,20]. We use a high-resolution onshore topographic dataset to resolve accurately the terrace uplift and flexural pattern. We then complete the onshore analysis with depth-converted offshore seismic data[21] to provide a unique integrated view of the flexure resulting from continental rifting. Based on these, numerical modelling allows us to resolve the primary rheological parameters controlling lithospheric deformation in such a young rift system. This study provides new constraints on the dynamics of the Corinth Rift system, critical for understanding both active deformation and its controlling mechanisms at thousand- to million-years timescales.

Uplifted Marine terraces

The outstanding flight of marine terraces in the Corinth Rift[19,20] is shaped similarly to the modern shoreline and uplifted to elevations of 400 m (Fig. 1 and Supplementary Fig. 1). These palaeo-shorelines have been used to describe the progressive uplift and flexure synchronous with main interglacial peaks[10]. Thus, their gradually deformed geometry may be used as a "palaeo-geodetic" strain marker, providing key observables to be reproduced by numerical modelling experiments that may help derive mechanical characteristics of the Corinth Rift's evolution.

The Corinth terraces are generally composed of abrasion surfaces in soft Plio-Quaternary marls, sandstones and conglomerates, and are unconformably overlain by 2-6 m of

erosion-resistant caprock consisting of well-cemented coastal deposits (Supplementary Fig. 2). In the area between Corinth and Xylokastro, we obtained a 2m-resolution Digital Surface Model (DSM) from Pleiades satellite imagery. This DSM allows us to quantify the 3D terrace geometry with far greater detail than a typical open-source Digital Elevation Model (Fig. 2; Supplementary Fig. 3).

The terraces are typically bounded inland by a palaeocliff. The intersection between terrace and palaeocliff, or shoreline angle (Supplementary Fig. 2), is considered the most appropriate datum of past sea-level position during the highstand they were formed[22,23]. We focus on the shoreline angles of terraces formed during major interglacial highstands (Fig. 3b), that are the widest and best preserved here[10] and globally[24], and have their corresponding glacio-eustatic sea-level less uncertain than lower interstadial highstands[25]. To determine which terraces correspond to interglacial highstands, we take into account available ages, and terrace width and preservation. We adopt the proposed terrace names by Armijo et al.[10], and distinguish previously undescribed sub-levels with Roman numerals. Our high-resolution analysis allows us to detect both small (down to ~1m) and strongly eroded cliffs, and hence more terrace sub-levels than previous. Sub-levels serve as guidelines for a precise spatial correlation across the whole flight of terraces, which increases the accuracy to determine the overall flexed terrace geometry and particularly the geometry of more eroded terrace levels older than the Old Corinth (II) (~240 ka). The shoreline angles determined for the wide and well-preserved terraces New Corinth (II) and Old Corinth (II) correlate unambiguously with the two first major interglacial highstands preceding the present-day one, Marine Isotope Stage (MIS) 5e (~124 ka) and MIS 7e (~240 ka) respectively (Fig. 3b), as supported by U/Th coral datings[26-28] and IcPD dating of *Pecten*[29]. Although our shoreline angle elevations and terrace mapping are more accurate, this correlation is in essence similar to the interpretation of Armijo et al.[10] However, our refined geometry and updated knowledge of glacio-eustatic sea-level variation[30] leads us to propose correlation of the Temple (II) and Laliotis terraces to interglacial highstands MIS 9e (~326 ka)

and MIS 11c (~409 ka) respectively, in better agreement than Armijo et al.[10] with assumed time-constant uplift rates (Supplementary Fig. 4). Using the same assumption, terraces older than the designated Unnamed and Nicoletto would correspond to MIS 13e (~505 ka) and MIS 15c (~605 ka) respectively (Fig. 3b), but these old levels are significantly degraded and laterally discontinuous. All of the other terrace levels should correspond to interstadial sea-level highstands lower than today's sea level. Those interstadial levels are more numerous and better preserved at ~2 km distance from the Xylokastro Fault (Fig. 2), where the footwall uplift rate is the highest observed (~1.3 $mm \cdot yr^{-1}$; Supplementary Fig. 4).

The first order signal of the best-preserved terraces indicates a broad footwall flexure of at least ~20 km in relation to the Xylokastro on- and offshore faults and Lykoporia Fault (Fig. 1 and 2). To estimate the long-term maximum footwall uplift rate at a hypothetical 0 km distance from the fault, we extrapolated the combined uplift rates of the New Corinth (II), Old Corinth (II), Temple (II) and Laliotis shoreline angles, obtaining an uplift rate of 1.63±0.12 $mm \cdot yr^{-1}$, or 1.72±0.08 $mm \cdot yr^{-1}$ if we exclude the slightly lower uplift rates of the New Corinth (II) terrace (Supplementary Fig. 4).

Rift-scale cross-section

Several sills, including the Rion sill in the western Gulf[31] and the Corinth Isthmus in the eastern Gulf (Fig. 1), presently onshore, limited the water exchange during sea-level lowstands between the Gulf and the open sea over the past 600-700 ka[17], resulting in alternating marine/lacustrine sedimentation found now both on- and offshore[17,18,32]. Long piston cores through the last lacustrine-marine transition ~13 ka[33] have been correlated to sharp changes in seismic character within seismic profiles. On the basis of this seismic character change, several studies have interpreted the base horizon of deeper high amplitude packages as older lacustrine-marine transitions and correlated these to glacio-eustatic sea-level curves[12,19,34,35] down to the basin-wide unconformity U (Fig. 3). We used the most recent interpretation of seismic stratigraphy,

faults and velocity model[35] to depth-convert seismic line L35 of Taylor et al.[21], and combined it with the onshore topography across the Klimenti Gilbert-type delta (hereafter Klimenti Delta) and the shoreline angles of major interglacial terrace levels (Fig. 3). The independently proposed timing of on- and offshore markers is remarkably similar. Small systematic differences of ~5-15 ka would thus correspond to delays between lacustrine to marine transitions and the maximum sea-level stands reached at the climax of interglacial periods (Fig. 3).

The cross-section suggests that ~60-70% of the deformation associated with the Xylokastro and Lykoporia faults has occurred over the past ~610 ka, assuming that the highest Klimenti Delta foresets onshore and deepest sediments offshore are age-equivalent to the onset of faulting. Before ~610 ka, detailed interpretation is hindered by the lack of well-developed marine terraces onshore and lack of clear seismic horizons offshore. The most elevated marine deposits in this area are found near Souli (Fig. 3), and have been tentatively dated as <450 ka[20] using nanoplankton. We are sceptical about this age for two reasons: 1) The paleontological evidence are rather weak as the age is based on the absence rather than the presence of a nanoplankton species; 2) If correct, it would imply a threefold deceleration of uplift rate with respect to the more reliably dated New and Old Corinth terraces (from ~2.1 to ~0.7 $mm \cdot yr^{-1}$ at 10 km from the fault). Northward fault migration has occurred in the western Corinth Rift[36], which could have locally lead to a sudden uplift rate deceleration, but the only major normal faults in this part of the Corinth Rift are the Xylokastro and Lykoporia faults, within a few kilometres distance from each other. Given the ~20 km uplift wavelength, simple migration of fault activity between these faults could not easily account for a threefold decrease in uplift rate at this distance from the fault. We do note the similarity in geometrical position between the highest marine deposits onshore and oldest marine incursion interpreted offshore (Souli/Nicoletto and horizon U; Fig. 3), which hints at brackish/lacustrine conditions before ~610 ka, and sea/lake level variations too subtle to produce marine terraces and markers in offshore sedimentation.

Linear extrapolation using the uplift rate of the interpreted terraces suggests an age for the Klimenti Delta (Fig. 3) of 1.0±0.1 Ma. Recent overview studies of the onshore stratigraphy have estimated its age as Middle Pleistocene[36], and slightly older as 2.0±0.2 Ma[37], the latter suggesting that a linear extrapolation from the terrace uplift rates might be too simple and uplift rates have been accelerating over the past ~2 Ma. Since those ages were based on indirect stratigraphic evidence rather than direct dating of the delta, we keep a broad estimate of 2.2-0.9 Ma for the initiation of the Xylokastro and/or Lykoporia Faults. The most elevated Gilbert-type delta in the Gulf, the Mavro Delta further west (Fig. 1), has been uplifted by the onshore Xylokastro and Dervenios faults (Figs. 1, 3). Comparing the Mavro and the Klimenti deltas, as well as their now inverted river drainage systems[38], we infer 1/3 more uplift for the Mavro than for the Klimenti delta (Fig. 3), and hence a slightly earlier onset of fault activity and/or higher average uplift rates.

We estimated the long-term slip rate and the uplift/subsidence (U:S) ratio by reconstructing the cross-section back to ~610 ka (Fig. 4). Palaeobathymetry in the Gulf ~610 ka is unknown, therefore in our reconstructions we apply a palaeobathymetry range from 800 m (todays maximum water depth) to 0 m, and correct for sediment compaction. The constant or slightly decelerating uplift rates onshore comparing New Corinth (II) to older terraces, and acceleration of subsidence rates offshore comparing H2 to older horizons (Supplementary Fig. 4), suggests a northward migration of fault activity (from Xylokastro to Lykoporia Fault, Fig. 3) affecting the most recent interglacial markers (~123-135 ka). Excluding those markers, and assuming most of the long-term deformation is related to the Xylokastro Fault, we estimate a long-term maximum subsidence rate of ~2.2-4 $mm \cdot yr^{-1}$ (Supplementary Fig. 4). Combining this with our long-term estimate of the maximum uplift rate from the marine terraces, and assuming the fault system is dipping 60° (Supplementary Fig. 5), we obtain a cumulative slip rate of 4.5-6.7 $mm \cdot yr^{-1}$ on the Xylokastro and Lykoporia faults and an U:S ratio of 1:1.2-2.4.

Fault modelling

The calculated U:S ratio is at variance with previous numerical fault models for Corinth that predicted 2.7-3.5 times more subsidence than uplift for this fault system, whereas other models that may have reproduced the U:S ratio better with inviscid rheologies beneath the upper crust[39,40], do not adequately describe the flexure geometry observed in the rift (Fig. 5a). Modelling studies of deformation in the western Gulf considered multiple faults[41,42] and resulted in flexure wavelengths dissimilar to those observed in our cross-section (Fig. 5a). Visco-elastic crustal-scale models[43] illustrated the importance of fault geometry to reproduce the first order U:S pattern observed in the Gulf, however these models did not account for crustal necking and neglected the role of the lithospheric mantle during flexure. This motivated an updated approach by incorporating visco-elastic lithosphere-scale models at high resolution. We follow the principle of King et al.[44] that geological and geomorphic structures are the cumulative result of many earthquake cycles, and use a finite element model to solve for the surface displacements resulting from imposed normal slip on a planar fault in a simplified layered lithosphere made of either 3 or 5 layers. The fault plane runs through an elastic upper crust overlying a visco-elastic lower crust and upper mantle (Supplementary Fig. 7). We choose to reproduce the uplift and flexure pattern of the Old Corinth terrace shoreline (II) over 240 ka, because its deformed geometry is particularly well preserved and dated. We do not attempt to precisely reproduce the depth to offshore markers, due to the uncertainty in palaeobathymetry at the time of their formation and effects of secondary faulting offshore, but we do show the range of likely depths for these markers (Fig. 5) defined by the estimated subsidence rates (Supplementary Fig. 4). Given the possible northward fault migration discussed in the previous section, we assume most of the deformation pre-dating ~135 ka is caused by the on- and offshore Xylokastro faults, and use the approximately perpendicular profile A-A' (Figs. 1, 3) as a reference section for our modelling, with the position of the onshore Xylokastro Fault as 0 m fault distance.

In Fig. 5b and Supplementary Table 1 we show the parameters that we found have a major influence on the resulting deformation pattern of the 3-layer models. Compared to the reference model (M1), all these parameters influence the width of the uplifted zone, whereas all parameters but the upper crustal thickness influence the U:S ratio. The curvature of the footwall flexure is mainly influenced by the Young's Modulus of the upper crust and the viscosity of the lower crust, increasing in flexure with lower and higher values, respectively. We show good fits to the data in Fig. 5c, using a 60° dipping fault as suggested from seismic data interpretation (Fig. 3; Supplementary Fig. 5), and a 10 km upper crustal thickness in agreement with the peak in microseismicity in this area of the Gulf (Supplementary Fig. 6). In our models we have used the range of possible slip rates from the previous section (4.5 – 6.7 $mm \cdot yr^{-1}$) and a regional uplift rate unrelated to rifting between 0-0.3 $mm \cdot yr^{-1}$ (see discussions in refs. [10,45]). Assuming the long-term Young's Modulus of the upper crust is comparable to typical values on coseismic timescales (see discussions in refs. [10, 44]), the lower crustal viscosity should be on the order of ~10^{23} Pa·s to reproduce the correct curvature of the terraces, and an upper mantle viscosity between $5 \cdot 10^{21}$ and $2 \cdot 10^{22}$ Pa·s is required to match reasonable slip rates and regional uplift rates (M8, M9 in Fig. 5c; Supplementary Fig. 7; Supplementary Table 2). Increasing the lower crustal viscosity by an order of magnitude has a similar effect on the curvature of the flexure as decreasing the upper crustal Young's Modulus by an order of magnitude, but the latter has a stronger effect on the U:S ratio (M2 and M5; Fig. 5b). It is difficult to get good fits to the data with an upper mantle viscosity lower than ~$3 \cdot 10^{21}$ Pa·s and a Young's Modulus and lower crustal viscosity lower than the values for M10 (Fig. 5c).

Previous studies on postseismic relaxation pointed out that models using only two homogeneous layers to represent the lower crust and upper mantle tend to result in a bias towards a relatively higher viscosity lower crust[46,47]. Therefore we also tested models in which we split both the lower crust and upper mantle in two separate layers, letting both the lower

crustal and upper mantle viscosity decrease with depth (Supplementary Fig. 8, Supplementary Table 2). Unlike the 3-layer models, these 5-layer models have the lowest misfits with the uplift pattern for similar lower crustal and upper mantle viscosities (M34 in Fig. 5c, Supplementary Table 2).

Despite good fits to the uplift pattern, all the models in Fig. 5c show a mismatch with the subsidence pattern. We attribute the mismatch in reproducing the offshore pattern to the presence of antithetic faults ~15 km north of the Xylokastro Fault (Figs. 3, 5), which modify the flexure pattern. We tested if the models were sensitive to earthquake recurrence times and modelling with fixed or moving sidewalls (M11-M13 in Supplementary Fig. 7), both of which do not influence our results. Additional models with a 15 km upper crustal thickness, 50° fault, elasto-plastic upper crust and non-linear (powerlaw) visco-elastic lower crust are discussed in the Supplementary Information (Supplementary Fig. 7 and Supplementary Table 1), but also do not change our main results.

Tectonic and rheological implications

Our revised slip rate of 4.5-6.7 $mm \cdot yr^{-1}$ for the combined Xylokastro/Lykoporia faults, based on both onshore and offshore data, and a 60° fault dip, is significantly lower than the previous estimate of 7.0-16 $mm \cdot yr^{-1}$ for this fault system[9]. The improvement to the slip rate estimate mainly results from the incorporation of the offshore data constraining hanging wall subsidence into the flexural model. If we assume the fault system is dipping ~40° instead[18], the cumulative slip rate would be 6.0-9.0 $mm \cdot yr^{-1}$, compatible with the previously estimated minimum rate of 7$mm \cdot yr^{-1}$ but still with a much lower upper bound. This discrepancy emphasizes the need to integrate on- and offshore data to estimate slip rates of major coastal fault systems, and thus for estimating potential earthquake recurrence and seismic hazards.

Compared to coseismic deformation, long-term patterns integrated over many earthquake cycles tend to have a lower U:S ratio and broader wavelength of deformation due to postseismic

relaxation processes of the deeper layers[44]. Few other studies have obtained long-term U:S ratios on crustal scale normal faults, but our estimate is in good agreement with the 1:1.2-2.2 estimate for the East Eliki Fault[48] (Fig. 1), and values of ~1:1-2.5 for normal faults in the Basin and Range[49]. The influence of the fault angle and upper crustal strength on this ratio has been pointed out by previous studies[10,44] and our study demonstrates that the rheology of the lower crust and upper mantle also plays a major role in controlling the surface deformation pattern. Unlike those studies, we do not require the long-term upper crustal strength to be lower than the short-term strength, or the effective elastic thickness to be smaller than the depth of the seismogenic layer.

The best-fitting 3-layer models for the terraces (Fig. 5c) have a lower crustal viscosity that is 2-20 times higher than the upper mantle viscosity. The relatively localised Moho rise (Fig. 5c) in these models is a direct consequence of this viscosity contrast, and is in good agreement with local Moho geometry (Supplementary Fig. 6). Our results agree well with compilations of postseismic relaxation studies on 10^0-10^3 yr timescales that also show lower crustal viscosities to be generally higher than upper mantle viscosities in 3-layer models[50,51], although ~1-3 orders of magnitude lower than our long-term viscosity estimates. Our tests on a 2.4 ka timescale (M28-M31 in Supplementary Fig. 7) fit within that context, showing that appropriate absolute viscosity values depend on the time period under consideration for relaxation, while the relative viscosity contrast remain immutable.

Within our 5-layer models (M34 in Fig. 5c, Supplementary Fig. 8), relatively localized Moho rise occurs across an inverse viscosity contrast with respect to the 3-layer models, but produces equally good-fitting results (Supplementary Table 2). These tests agree with findings on postseismic relaxation studies showing that 3-layer models are biased towards higher viscosity lower crust[46,47], but on a 240 ka timescale. Our 5-layer models achieve the best fits to the data with similar viscosity lower crust and upper mantle, and increasing the amount of layers even more may also permit a good fit to the data with an upper mantle stronger than the lower crust.

As a consequence, our models cannot unequivocally demonstrate that the lower crust in the Corinth Rift is stronger or weaker than the upper mantle. What the best-fitting 3- and 5-layer models do have in common is that most of the viscous relaxation takes place relatively deep, in the lower portion of the lower crust and/or upper mantle (Fig. 5d). Coming back to primary observations within our cross-section of the Corinth Rift this is both intuitive and physically reasonable: viscous relaxation allows for higher U:S ratios with respect to coseismic elastic flexure, whereas its relatively deep occurrence allows for the topographic signal of coseismic elastic flexure to be well maintained at the surface throughout many earthquake cycles. Since the few other long-term U:S ratio estimates for normal faults[48,49] are similar to that we obtain for the Corinth Rift, and its record of flexure geometry is unparalleled worldwide, this topographic evolution controlled by rheological layering may well typify rapid localised extension of continental lithosphere.

Methods

Marine terrace analysis

To develop the DSM, we obtained tri-stereo Pleiades satellite images of 0.5m-resolution covering the terrace sequence between Xylokastro and Corinth. The open-source software MicMac[54,55] was used to create tie-points, orientate the images and calculate a 0.5m-resolution DSM, using ground control points at 0 m elevation for several locations along the coastline. To reduce the topographic effects of vegetation, crops and man-made structures, the DSM was downsampled to 2 m resolution (Fig. 2).

Mapping of the terraces (Figs. 1, 2 and Supplementary Fig. 1) was done semi-automatically using the surface classification model of Bowles and Cowgill[56], which combines the slope and roughness linearly to detect relatively low-slope smooth surfaces. Contours around those surfaces were drawn manually using a combination of satellite imagery, slope maps and

hillshade images of the DSM. The slope of the Holocene seacliff was measured at 48 locations and its value ±1σ was used to estimate the horizontal and vertical position of the shoreline angles for ~700 palaeocliffs with TerraceM8[57,58] (Supplementary Fig. 2 and Supplementary Fig. 9). To reduce the influence of fluvial and gravitational erosion, we used the maximum topography of 100m-wide swath profiles perpendicular to the cliffs, the size preferred by Jara-Muñoz et al.[58]. All swath profile and shoreline angle locations are included as supplementary Google Earth and ESRI Shapefile data files. The terraces were correlated laterally using satellite imagery, mapview and profile view of shoreline angles in combination with a N130°E coast-parallel swath stack[59] of 500 average elevations of swath profiles (Fig. 2d).

The uplift rate *U* for individual shoreline angles was calculated using $U = (H_T - H_{SL})/T$, where H_T is the present elevation above the modern mean sea-level, H_{SL} is the eustatic sea-level elevation for the time interval of terrace formation and T is the age of terrace formation. Following Gallen et al.[60], standard errors SE were calculated using:

$$SE(u)^2 = u^2 \left(\left(\frac{{\sigma_H}^2}{(H_T - H_{SL})^2} \right) + \left(\frac{{\sigma_T}^2}{T^2} \right) \right) \quad (1)$$

where σ_H is the combined uncertainty of shoreline angle elevation and eustatic sea-level correction, and σ_T is the uncertainty in age of terrace formation. For the eustatic sea-level highstands MIS 5e, MIS 7e, MIS 9e and MIS 11c, correlated to the New Corinth (II), Old Corinth (II), Temple (II) and Laliotis terraces, we used the eustatic highstand age uncertainty of 123.5±8.5 ka, 240±6 ka, 326±9 ka and 409±16 ka[61] to represent the uncertainty in age of terrace formation. As eustatic sea-level corrections for those same highstands we used 5.5±3.5 m, 0.5±3.5 m, 2.5±5.5 m and 5±8 m[30] , and added these uncertainties to the uncertainties calculated for each individual shoreline angle (Supplementary Fig. 2 and Supplementary Fig. 9). The uplift rate at the onshore Xylokastro Fault was estimated by combining the New Corinth (II), Old Corinth (II), Temple (II) and Laliotis uplift rates and extrapolating a best fitting quadratic

curve with Matlab® (Supplementary Fig. 4). A critical χ^2 test was done to confirm that the residuals follow a Gaussian distribution and the uplift rate dataset is well described by the curve[62], which was the case when excluding the New Corinth (II) terrace, but not when including that terrace. Within this test we excluded the New Corinth (II) datapoints between 13 and 18 km distance from the fault, since their elevation appears to be disturbed by sedimentary processes on the Vokha plain (Fig. 1), particularly around rivers.

Constructing cross-section and evolution model

We depth-converted the multi-channel seismic section L35[21] using the velocity model of Taylor et al.[21], and adopted the interpretation of faults and seismic horizons from Nixon et al.[35] (Supplementary Fig. 5). The shoreline angles were reprojected on a profile of the same orientation as the seismic section, approximately perpendicular to the on- and offshore Xylokastro Fault (Fig. 1 and Fig. 3). To combine the terraces with topsets of the overlying Klimenti Delta the maximum elevation of a 4-km wide, N025E oriented swath profile was also reprojected along the same line (Fig. 1). The river profile of the inverted Safenatos River and the windgap-connected trunk of the Trikalitikos river were merged together, and horizontally scaled to have the windgap at the correct location within the cross-section and the river outlet at the coastline. Best-fitting quadratic curves for the New Corinth (II), Old Corinth (II), Temple (II) and Laliotis terraces were extracted with Matlab®. The Laliotis curve, assuming an age of 409 ka and a eustatic sea-level correction of +5 m, was extrapolated linearly to estimate total uplift at 605 ka and 1050 ka, approximately corresponding to the sea-level highstand following the oldest marine incursion interpreted offshore (Fig. 3b) and the age to match the position of the Klimenti Delta overlying the terrace sequence (Fig. 3a). The sill depth is chosen at 62 m[31], and for simplicity chosen as constant through time. Given the fast rate of sea-level rise before major interglacial highstands, uncertainty in sill depth does not change the age of the interpreted offshore horizons much, nor does the depth-uncertainty in the sea-level curve. We chose to

display the sea-level curve of Bates et al.[53] since it is the most recent curve that we are aware of covering >610 ka that is accounting for global observations of uplifted palaeoshorelines, and use their equatorial Pacific curve since they use it as reference curve. For the background topography comprising the Mavro Delta (Fig. 3c) we used a 4-km wide swath profile along the same orientation as A-A'.

In the evolution model (Fig. 4) the palaeodepth of the Corinth Gulf at 605 ka was chosen at 400 m as an average of two end-member scenarios at which seismic horizon U would represent the sea-level at 0 m, or the local sea bottom at its present-day depth of ~800 m. Sea/lake deepening was assumed to be constant between 605 ka and present, and sediments were decompacted using a porosity-depth relationship for calcareous sediments from Nixon et al.[35], based on experimental data[63]. To calculate a subsidence rate over the past ~610 ka we estimated the subsidence of seismic horizon U, taking end-member scenarios of 0 and 800 m palaeo sea/lake depth into account. We used the current depth of seismic horizon U of ~2480 m depth, substracting 0-800 m for the sea/lake palaeodepth and 415-312 m due to compaction of the sediments below the U horizon. The same principle was applied for every individual horizon in Supplementary Fig. 4, and used for the error margins in Fig. 5 and Supplementary Fig. 7. Since reconstruction of the maximum swath profile topography from Fig. 3 should be relatively insensitive to river incision, we did not take into account onshore erosion processes in Fig. 4.

Fault modelling

For the fault modelling we used PyLith[64], an open-source finite element code for dynamic and quasi-static simulations of crustal deformation. We used a starting model with a 10 km upper crustal thickness, adopting the peak in microseismicity depth (Supplementary Fig. 6) around the cross-section of Fig. 3, and a 35 km crustal thickness following Moho depth estimates from Ps receiver functions[65] and tomographic inversion of PmP reflection times[66]. Listric and biplanar fault geometries were excluded from our models, since they are not expected to give the

significant footwall uplift that our data suggests[43]. For model simplicity we exclude erosion and sedimentation processes, to which previous numerical models with much lower upper crustal Young Modulus were relatively insensitive[10]. We used 2.5 m normal slip earthquakes with a recurrence time of 500 years, following our range of estimated long-term slip rates, and roughly in agreement with the recurrence times for major earthquakes inferred from offshore palaeoseismology[67]. The models have uniform slip until the base of the upper crust, linearly decreasing to 0 m slip between 10 and 12 km depth to avoid extreme boundary effects at the fault tip. Sensitivity tests suggest the models are insensitive to the recurrence time if the slip rate is the same, and the ground surface pattern for different slip rates can be approximated by linear inter- or extrapolation of the displacement vector after the model run (Supplementary Fig. 7). For the models with moving walls we applied a 1.25 mm/yr horizontal velocity for both walls to ensure all extension in the model is taken up by the 5 mm/yr slip along the fault. We applied an upward velocity of 0.03 mm/yr to isostatically compensate for the thinning of the crust. For the models with an elastoplastic upper crust (Supplementary Fig. 7) we used the plastic parameters from Cianetti et al.[42] and for the models with a non-linear (powerlaw) viscoelastic lower crust we used the quartz flow law from Gleason and Tullis[68]. For the five-layer models we used similar parameters to the starting model, and systematically varied viscosities between $3 \cdot 10^{21}$ and $5 \cdot 10^{23}$ Pa·s (Supplementary Fig. 8, Supplementary Table 2), which is a similar range to our best fitting 3-layer models (Fig. 5c). In all model runs we included gravitational body forces and used a finite strain formulation.

For the comparison with previous numerical models (Fig. 5a) we vertically rescaled the deformation pattern of selected models in those studies to approximately match the Old Corinth (II) terraces. From Armijo et al.[10] this is their figure 23, from Bott et al.[39] this is the model in their figure 7b with an appropriate U:S ratio, from Lavier et al.[40] this is the model in their figure 2 (bottom) and from Cianetti et al.[42] this is the model in their figure 3b with an appropriate U:S ratio. Le Pourhiet et al.[41] argue in their text for ~2.0 $mm \cdot yr^{-1}$ of regional uplift, and given the

complicated multi-fault deformation pattern in their preferred model in their Figure 8d we did not apply this correction, nor did we scale it vertically to the Old Corinth (II) terraces.

References

1. Kusznir, N. J. & Park, R. G. The extensional strength of the continental lithosphere: its dependence on geothermal gradient, and crustal composition and thickness. *Geological Society, London, Special Publications* **28,** 35–52 (1987).
2. King, G. C. P. *et al.* The evolution of the Gulf of Corinth (Greece): an aftershock study of the 1981 earthquakes. *Geophys. J. Int.* **80,** 677–693 (1985).
3. Nishimura, T. Rheology of the lithosphere inferred from postseismic uplift following the 1959 Hebgen Lake earthquake. *J. Geophys. Res.* **108,** (2003).
4. Gourmelen, N. & Amelung, F. Postseismic mantle relaxation in the Central Nevada Seismic Belt. *Science* **310,** 1473–1476 (2005).
5. Lambotte, S. *et al.* Reassessment of the rifting process in the Western Corinth Rift from relocated seismicity. *Geophys. J. Int.* **197,** 1822–1844 (2014).
6. Buck, W. R. Flexural rotation of normal faults. *Tectonics* **7,** 959–973 (1988).
7. Jackson, J. A. & White, N. J. Normal faulting in the upper continental crust: observations from regions of active extension. *J. Struct. Geol.* **11,** 15–36 (1989).
8. Watts, A. B. & Burov, E. B. Lithospheric strength and its relationship to the elastic and seismogenic layer thickness. *Earth Planet. Sci. Lett.* **213,** 113–131 (2003).
9. Huismans, R. & Beaumont, C. Depth-dependent extension, two-stage breakup and cratonic underplating at rifted margins. *Nature* **473,** 74–78 (2011).
10. Armijo, R., Meyer, B., King, G. C. P., Rigo, A. & Papanastassiou, D. Quaternary evolution of the Corinth Rift and its implications for the Late Cenozoic evolution of the Aegean. *Geophys. J. Int.* **126,** 11–53 (1996).

11. Rohais, S., Eschard, R., Ford, M., Guillocheau, F. & Moretti, I. Stratigraphic architecture of the Plio-Pleistocene infill of the Corinth Rift: Implications for its structural evolution. *Tectonophysics* **440,** 5–28 (2007).
12. Bell, R. E. *et al.* Fault architecture, basin structure and evolution of the Gulf of Corinth Rift, central Greece. *Basin Res.* **21,** 824–855 (2009).
13. Raymo, M. E., Oppo, D. W. & Curry, W. The Mid-Pleistocene climate transition: A deep sea carbon isotopic perspective. *Paleoceanography* **12,** 546–559 (1997).
14. Medina-Elizalde, M. & Lea, D. W. The mid-Pleistocene transition in the tropical Pacific. *Science* **310,** 1009–1012 (2005).
15. Roberts, G. P. *et al.* Localization of Quaternary slip rates in an active rift in 10^5 years: An example from central Greece constrained by ^{234}U-^{230}Th coral dates from uplifted paleoshorelines. *J. Geophys. Res.* **114,** (2009).
16. Beckers, A. *et al.* Influence of bottom currents on the sedimentary processes at the western tip of the Gulf of Corinth, Greece, *Marine Geology* **378,** 312-332 (2016).
17. Heezen, B. C., Ewing, M. & Johnson, G. L. The Gulf of Corinth floor. *Deep Sea Research and Oceanographic Abstracts* **13,** 381–411 (1966).
18. Collier, R. E. L. L. Eustatic and tectonic controls upon Quaternary coastal sedimentation in the Corinth Basin, Greece. *J. Geol. Soc. London* **147,** 301–314 (1990).
19. Dufaure, J.-J. & Zamanis, A. Un vieux problème géomorphologique : les niveaux bordiers au sud du Golfe de Corinthe (An old geomorphological problem : the levels developed on the southern border of the Gulf of Corinth). *Bulletin de l'Association de géographes français* **56,** 341–350 (1979).
20. Keraudren, B. & Sorel, D. The terraces of Corinth (Greece) — A detailed record of eustatic sea-level variations during the last 500,000 years. *Mar. Geol.* **77,** 99–107 (1987).
21. Taylor, B. *et al.* The structures, stratigraphy and evolution of the Gulf of Corinth rift, Greece. *Geophys. J. Int.* **185,** 1189–1219 (2011).

22. Lajoie, K. R. Coastal tectonics. *Active tectonics* (1986).
23. Scott, A. & Pinter, N. Extraction of Coastal Terraces and Shoreline-Angle Elevations from Digital Terrain Models, Santa Cruz and Anacapa Islands, California. *Phys. Geogr.* **24,** 271–294 (2003).
24. Pedoja, K. *et al.* Coastal staircase sequences reflecting sea-level oscillations and tectonic uplift during the Quaternary and Neogene. *Earth-Sci. Rev.* **132,** 13–38 (2014/5).
25. Caputo, R. Sea-level curves: Perplexities of an end-user in morphotectonic applications. *Glob. Planet. Change* **57,** 417–423 (2007).
26. Collier, R. E. L., Leeder, M. R., Rowe, P. J. & Atkinson, T. C. Rates of tectonic uplift in the Corinth and Megara Basins, central Greece. *Tectonics* **11,** 1159–1167 (1992).
27. Dia, A. N., Cohen, A. S., O'Nions, R. K. & Jackson, J. A. Rates of uplift investigated through 230Th dating in the Gulf of Corinth (Greece). *Chem. Geol.* **138,** 171–184 (1997).
28. Leeder, M. R. *et al.* Normal faulting and crustal deformation, Alkyonides Gulf and Perachora peninsula, eastern Gulf of Corinth rift, Greece. *J. Geol. Soc. London* **162,** 549–561 (2005).
29. Pierini, F., Demarchi, B., Turner, J. & Penkman, K. Pecten as a new substrate for IcPD dating: The quaternary raised beaches in the Gulf of Corinth, Greece. *Quat. Geochronol.* **31,** 40–52 (2016/2).
30. Murray-Wallace, C. V. & Woodroffe, C. D. *Quaternary Sea-Level Changes: A Global Perspective*. (Cambridge University Press, 2014).
31. Perissoratis, C., Piper, D. J. W. & Lykousis, V. Alternating marine and lacustrine sedimentation during late Quaternary in the Gulf of Corinth rift basin, central Greece. *Mar. Geol.* **167,** 391–411 (2000).
32. Palyvos, N. *et al.* Geomorphological, stratigraphic and geochronological evidence of fast Pleistocene coastal uplift in the westernmost part of the Corinth Gulf Rift (Greece). *Geol. J.* **45,** 78–104 (2010).

33. Moretti, I. *et al.* Sedimentation and subsidence rate in the Gulf of Corinth: what we learn from the Marion Dufresne's long-piston coring. *C. R. Geosci.* **336,** 291–299 (2004).
34. Sachpazi, M., Clément, C., Laigle, M., Hirn, A. & Roussos, N. Rift structure, evolution, and earthquakes in the Gulf of Corinth, from reflection seismic images. *Earth Planet. Sci. Lett.* **216,** 243–257 (2003).
35. Nixon, C. W. *et al.* Rapid spatiotemporal variations in rift structure during development of the Corinth Rift, central Greece. *Tectonics* **35,** 1225–1248 (2016).
36. Ford, M., Hemelsdaël, R., Mancini, M. & Palyvos, N. Rift migration and lateral propagation: evolution of normal faults and sediment-routing systems of the western Corinth rift (Greece). *Geological Society, London, Special Publications* SP439.15 (2016).
37. Gawthorpe, R. L. *et al.* Tectono-sedimentary evolution of the Plio-Pleistocene Corinth rift, Greece. *Basin Research,* 1-32, (2017).
38. Fernández-Blanco, D., De Gelder, G., Gallen, S. F., Lacassin, R. & Armijo, R. Transient rivers characterize evolving crustal-scale flexure in the Corinth Rift. *EarthArXiv Preprint*, (2017)
39. Bott, M. H. P. Modeling the formation of a half graben using realistic upper crustal rheology. *J. Geophys. Res.* **102** (B11), 24,605-24,617 (1997)
40. Lavier, L. L., Buck, W. R. & Poliakov, A. N. B. Self-consistent rolling-hinge model for the evolution of large-offset low-angle normal faults. *Geology* **27** (12), 1127-1130 (1999).
41. Le Pourhiet, L., Burov, E. & Moretti, I. Rifting through a stack of inhomogeneous thrusts (the dipping pie concept). *Tectonics* **23**, (2004)
42. Cianetti, S., Tinti, E., Giunchi, C. & Cocco, M. Modelling deformation rates in the western Gulf of Corinth: rheological constraints. *Geophys. J. Int.* **174,** 749–757 (2008).
43. Bell, R. E., Duclaux, G., Nixon, C. W., Gawthorpe, R. L. & McNeill, L. C. High-angle, not low-angle, normal faults dominate early rift extension in the Corinth Rift, central Greece. *Geology* **46** (2), 115–118 (2018).

44. King, G. C. P., Stein, R. S. & Rundle, J. B. The Growth of Geological Structures by Repeated Earthquakes 1. Conceptual Framework. *J. Geophys. Res.* **93,** 13307–13318 (1988).
45. Turner, J. A. *et al.* Testing rival tectonic uplift models for the Lechaion Gulf in the Gulf of Corinth rift. *J. Geol. Soc. London* **167,** 1237–1250 (2010).
46. Riva, R. E. M. & Govers, R. Relating viscosities from postseismic relaxation to a realistic viscosity structure for the lithosphere. *Geophys. J. Int.* **176,** 614–624 (2009).
47. Hines, T. T. & Hetland, E. A. Bias in estimates of lithosphere viscosity from interseismic deformation. *Geophys. Res. Lett.* **40,** 4260–4265 (2013).
48. McNeill, L. C., Collier, R. E. L., De Martini, P. M., Pantosti, D. & D'Addezio, G. Recent history of the Eastern Eliki Fault, Gulf of Corinth: geomorphology, palaeoseismology and impact on palaeoenvironments. *Geophys. J. Int.* **161,** 154–166 (2005).
49. King, G. C. P., Stein, R. S. & Rundle, J. The growth of geological structures by repeated earthquakes, 2: Field examples of continental dip-slip faults. *J. Geophys. Res.* **93,** 13319–13331 (1988).
50. Thatcher, W. & Pollitz, F. F. Temporal evolution of continental lithospheric strength in actively deforming regions. *GSA Today* **18,** 4 (2008).
51. Wright, T. J., Elliott, J. R., Wang, H. & Ryder, I. Earthquake cycle deformation and the Moho: Implications for the rheology of continental lithosphere. *Tectonophysics* **609,** 504–523 (2013).
52. De Martini, P. M. *et al.* Slip rates of the Aigion and Eliki Faults from uplifted marine terraces, Corinth Gulf, Greece. *C. R. Geosci.* **336,** 325–334 (2004).
53. Bates, S. L., Siddall, M. & Waelbroeck, C. Hydrographic variations in deep ocean temperature over the mid-Pleistocene transition. *Quat. Sci. Rev.* **88,** 147–158 (2014).

References Methods

54. Rosu, A.-M., Pierrot-Deseilligny, M., Delorme, A., Binet, R. & Klinger, Y. Measurement of ground displacement from optical satellite image correlation using the free open-source software MicMac. *ISPRS J. Photogramm. Remote Sens.* **100,** 48–59 (2015/2).
55. Rupnika, E., Deseillignya, M. P., Delorme, A. & Klinger, Y. Refined satellite image orientation in the free open-source photogrammetric tools Apero/Micmac. *ISPRS Annals of Photogrammetry, Remote Sensing & Spatial Information Sciences* **3,** (2016).
56. Bowles, C. J. & Cowgill, E. Discovering marine terraces using airborne LiDAR along the Mendocino-Sonoma coast, northern California. *Geosphere* **8,** 386–402 (2012).
57. Gelder, D. *et al.* Corinth terraces re-visited: Improved paleoshoreline determination using Pleiades-DEMs. *Geotectonic Research* **97,** 12–14 (2015).
58. Jara-Muñoz, J., Melnick, D. & Strecker, M. R. TerraceM: A MATLAB® tool to analyze marine and lacustrine terraces using high-resolution topography. *Geosphere* **12,** 176–195 (2016).
59. Armijo, R., Lacassin, R., Coudurier-Curveur, A. & Carrizo, D. Coupled tectonic evolution of Andean orogeny and global climate. *Earth-Sci. Rev.* **143,** 1–35 (2015/4).
60. Gallen, S. F. *et al.* Active simultaneous uplift and margin-normal extension in a forearc high, Crete, Greece. *Earth Planet. Sci. Lett.* **398,** 11–24 (2014).
61. Masson-Delmotte, V. *et al.* EPICA Dome C record of glacial and interglacial intensities. *Quat. Sci. Rev.* **29,** 113–128 (2010/1).
62. Trauth, M. H. *MATLAB® Recipes for Earth Sciences:* (Springer Berlin Heidelberg, 2015).
63. Goldhammer, R. K. Compaction and decompaction algorithms for sedimentary carbonates. *J. Sediment. Res.* **67,** (1997).
64. Aagaard, B., Williams, C. & Knepley, M. PyLith: A finite-element code for modeling quasi-static and dynamic crustal deformation. *Eos Trans. AGU* **89,** (2008).
65. Pearce, F. D. (Seismic imaging of the western Hellenic subduction zone : the relationship between slab composition, retreat rate, and overriding lithosphere genesis. (PhD thesis

Massachusetts Institute of Technology, 2015).

66. Zelt, B. C., Taylor, B., Sachpazi, M. & Hirn, A. Crustal velocity and Moho structure beneath the Gulf of Corinth, Greece. *Geophys. J. Int.* **162,** 257–268 (2005).
67. Campos, C. *et al.* Deciphering hemipelagites from homogenites through anisotropy of magnetic susceptibility. Paleoseismic implications (Sea of Marmara and Gulf of Corinth). *Sediment. Geol.* **292,** 1–14 (2013).
68. Gleason, G. C. & Tullis, J. A flow law for dislocation creep of quartz aggregates determined with the molten salt cell. *Tectonophysics* **247,** 1–23 (1995).

Acknowledgements

We thank Aurélia Hubert-Ferrari and two anonymous reviewers for commenting on an earlier version of the manuscript. The research leading to these results has received funding from the People Programme (Marie Curie Actions) of the European Union's Seventh Framework Programme under the ITN project ALErT (Grant FP7-PEOPLE-2013-ITN number 607996) and by the ISIS program of CNES. The authors thank Arthur Delorme for his technical assistance in producing the DSMs, and Raphaël Grandin for discussing an earlier version of the manuscript. Numerical computations for the DSM were performed on the S-CAPAD platform, Institut de Physique du Globe de Paris (IPGP), France. Seismic reflection data from EW0108 is available from the Marine Geoscience Data System.

Author contributions

G.D.G., D.F.-B. and R.L. designed the study, D.F.-B. produced the map and stacked swath, G.D.G. and R.A. mapped the marine terraces and performed their analysis together with D.M. and J.J.-M. R.E.B. depth-converted the seismic section, G.D.G. and G.D. performed the

numerical fault modelling. All authors discussed the results at different stages of the process. G.D.G. wrote the paper with contributions and edits from all other authors.

Competing Financial Interests statement

The authors declare no competing financial interests.

Data availability

The Pleiades satellite imagery was obtained through the ISIS and Tosca programs of the Centre National d'Etudes Spatiales (CNES, France) under an academic license and is not for open distribution. On request, we'll provide the DSM calculated from this imagery to any academic researcher who gets approval from CNES (contact isis-pleiades@cnes.fr for quoting this paper, and with lacassin@ipgp.fr in copy). The other data that support the findings of this study are available within the publication, referenced studies and/or from the corresponding author on request.

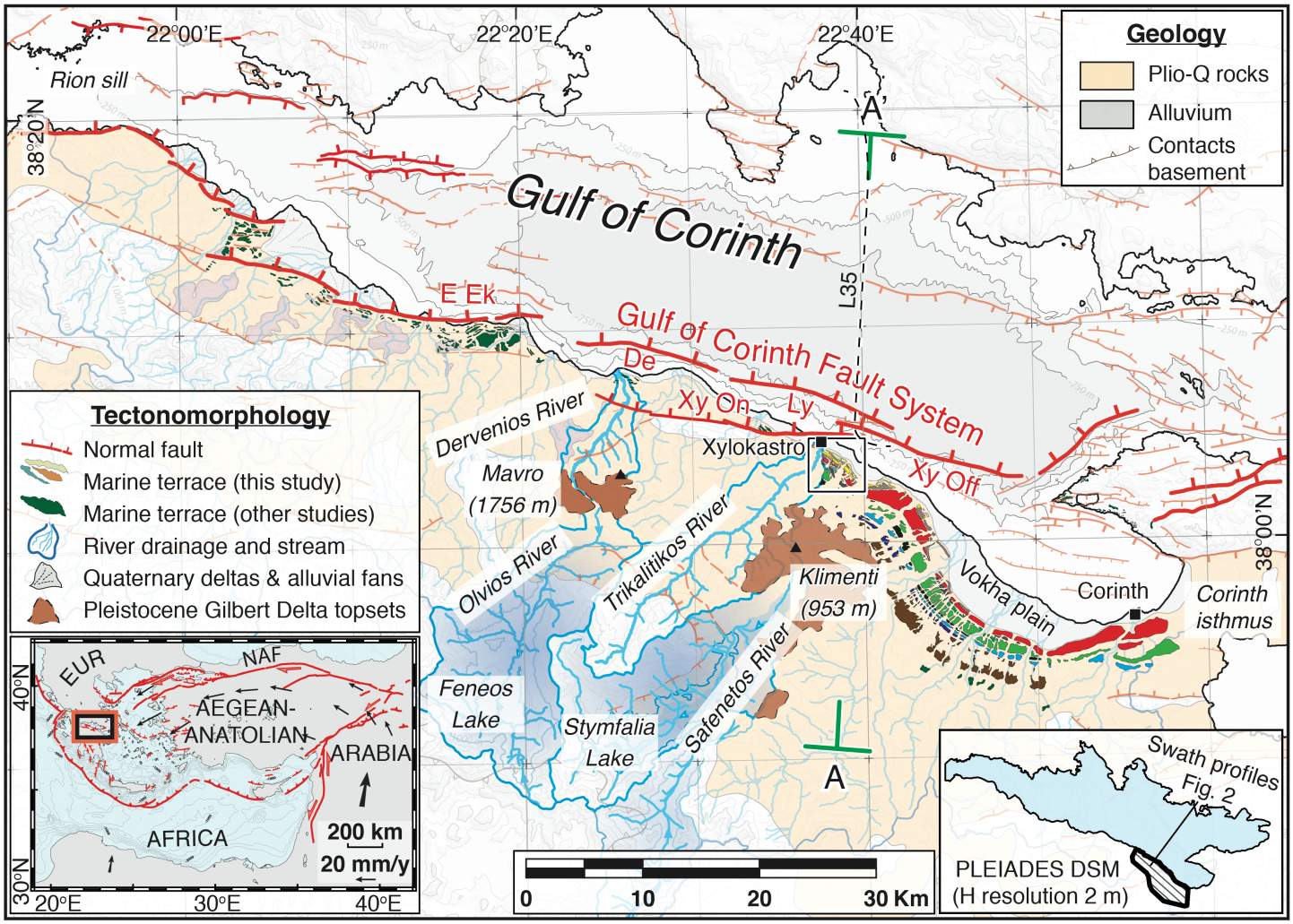

Figure 1: Active tectonics in the Gulf of Corinth. Solid box outlines location of Fig. 2, and A-A' indicates cross-section location for Fig. 3. Faults mentioned in the text are the East Eliki (E Ek), Dervenios (De), Lykoporia (Ly) and Xylokastro on- and offshore faults (Xy On and Xy Off). Marine terraces from other studies have been adopted from refs 10,15 and 52. Map was made using MAPublisher® version 9.8 (http://www.avenza.com/help/mapublisher/9.8/).

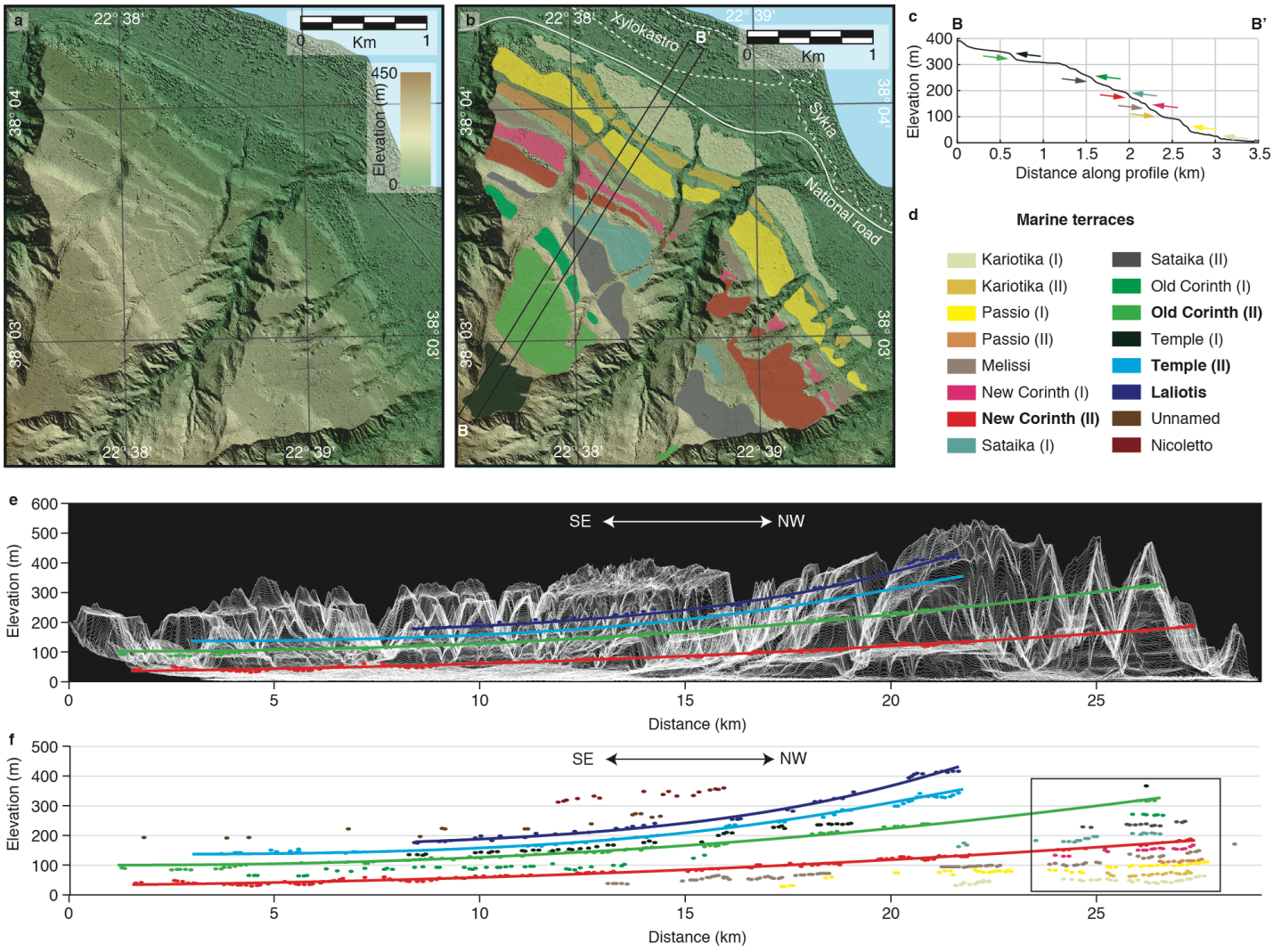

Figure 2: Detail of marine terraces on Pleiades DSM (a) Coloured hillshade DSM without interpretation, location given by inset in Fig. 1 **(b)** Same DSM with contouring of marine terraces **(c)** Average swath topography through marine terraces levels, location given by inset in **b** Arrows indicate differentiated terraces, colors indicated in **d (d)** Marine terrace legend, bold terraces are highlighted in **e**, **f** and Fig. 3 **(e)** Topography "view" parallel to the coast derived using stacked swath profiles with the shoreline angles and best fitting quadratic curves for the New Corinth (II), Old Corinth (II), Temple (II) and Laliotis terraces **(f)** All determined shoreline angles along the same profile. Box shows location of **a** and **b**. Maps were made using MAPublisher® version 9.8 (http://www.avenza.com/help/mapublisher/9.8/).

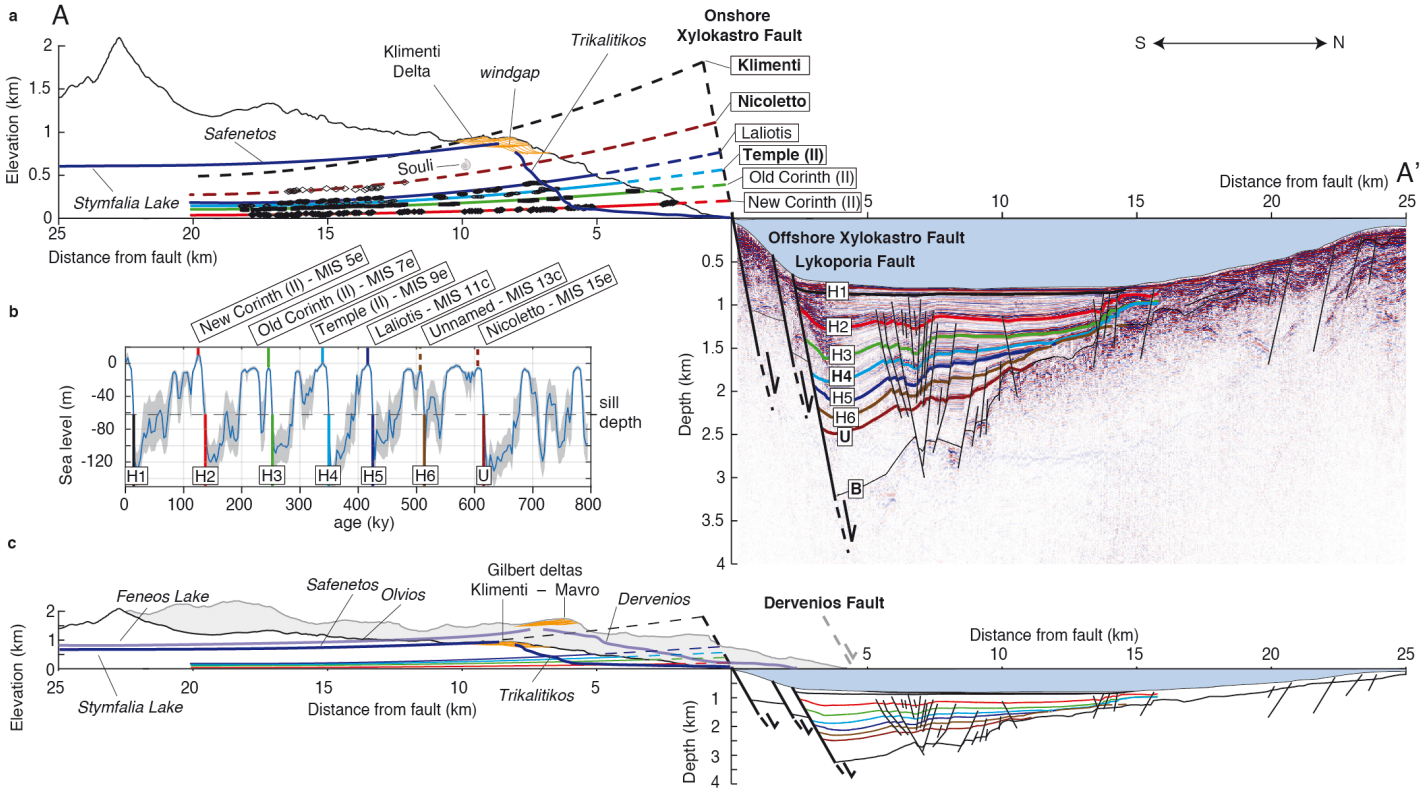

Figure 3: Combined on-offshore cross-section through Corinth Rift. (a) Cross-section with 3x vertical exaggeration, showing maximum topography of a 4-km wide swath profile across the Xylokastro terraces (Fig. 2a, b) and top of the Klimenti Delta (Fig. 1), shoreline angles of terraces assigned to major sea level highstands with best-fitting quadratic curves and part of the Trikalitikos-Safenetos river system, all reprojected on line A-A' of Fig. 1. Offshore seismic section is the interpretation of Nixon et al.[35] on the depth-converted line L35 from Taylor et al.[21] **(b)** Inferred ages of marine terrace levels and offshore seismic horizons plotted on the Pacific sea level curve of Bates et al.[53] **(c)** Main features of **a** without vertical exaggeration, and including the maximum topography of a 4-km wide swath profile parallel to A-A' across the Mavro Delta.

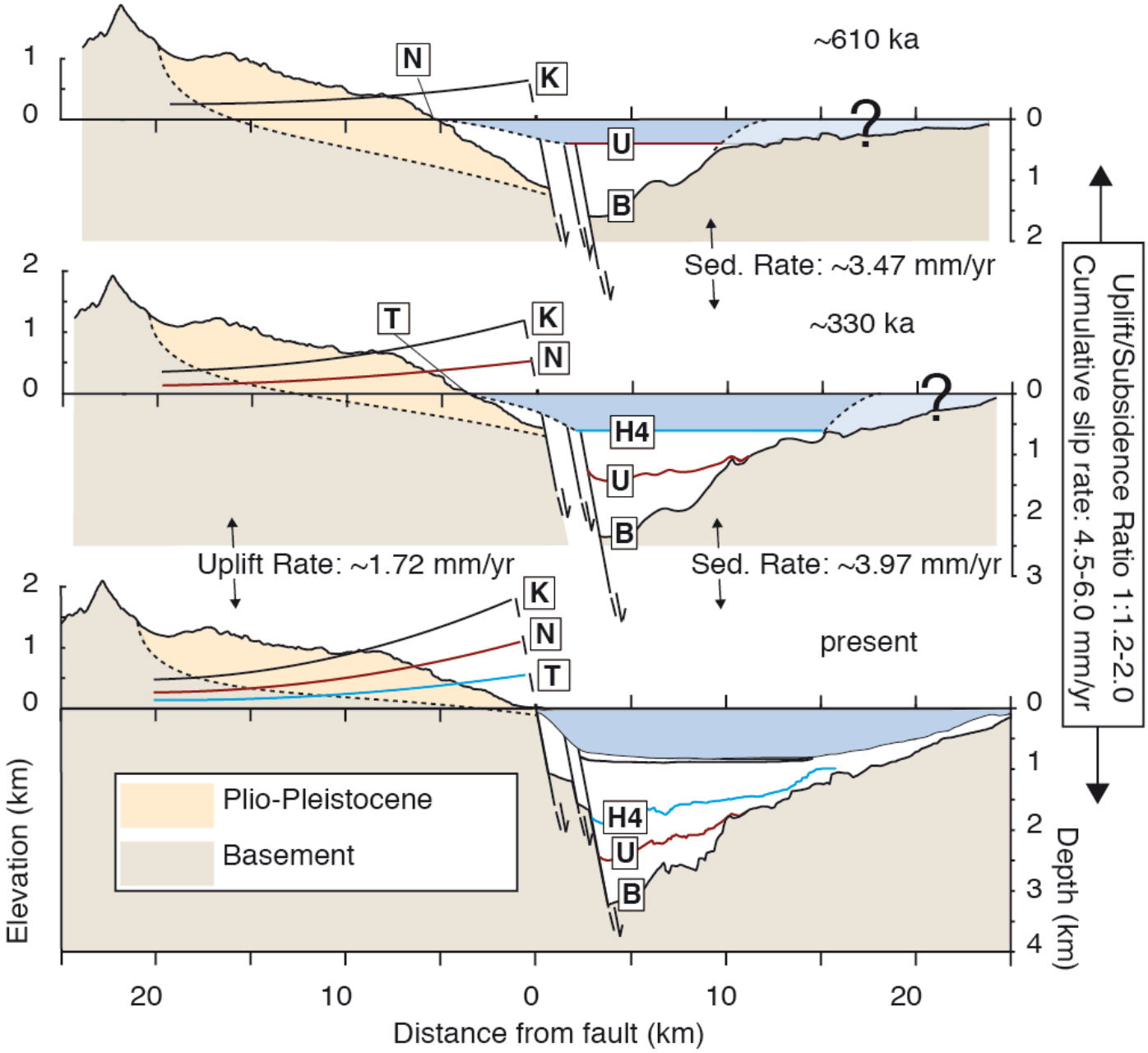

Figure 4: Schematic geologic restoration. The bold-labelled terraces and seismic horizons from Fig. 3 rotated back to horizontal, with the same rotation applied to the topo-bathymetry, accounting for sediment compaction.

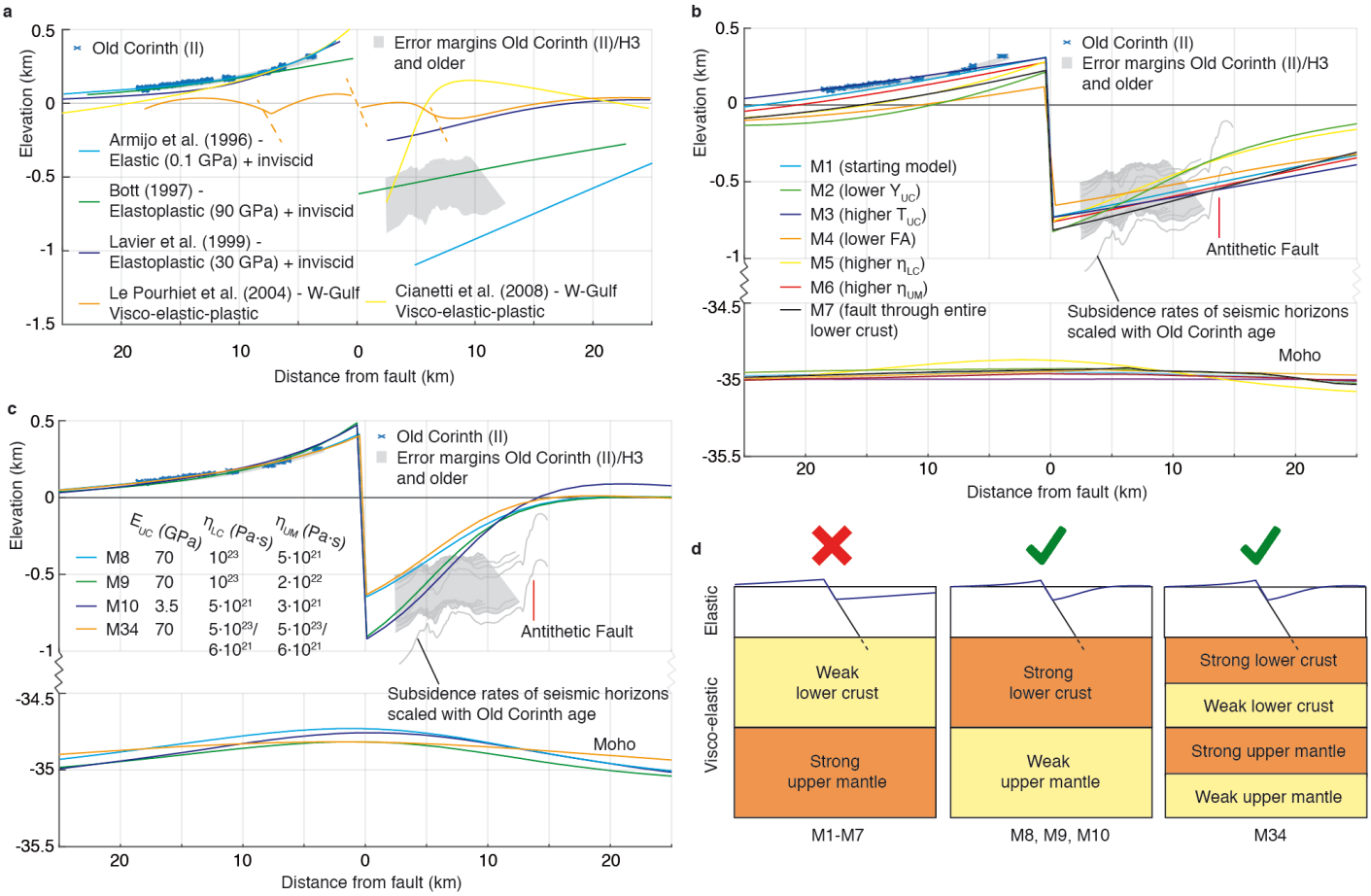

Figure 5: Fault modelling results. (a) Previous models within the Corinth Rift[10,41,42] and two other models with inviscid lower crust[39,40], all but Le Pourhiet et al.[41] vertically scaled to the elevation of the Old Corinth (II) marine terrace (see methods) **(b)** Sensitivity tests for the different model parameters compared to the Old Corinth (II) terrace. EUC = Young's Modulus of upper crust, TUC = thickness of upper crust, FA = fault dip angle, ηLC = viscosity of lower crust, ηUM = viscosity of upper mantle. **(c)** Best-fitting models, which reproduce fault flexure by a relatively high viscosity lower crust (models 8 and 9) or an upper crust with relatively low Young's Modulus (model 10). Model 8 has a slip rate of 4.5 mm·yr-1 and 0 mm·yr-1 of regional uplift rate, models 9 and 10 have a slip rate of 5.5 mm·yr-1 and 0.27 mm·yr-1 of regional uplift rate. Model 34 is the best-fitting model with 5 layers, in which the lower crust and upper mantle have the same viscosity, and is plotted here with a slip rate of 4.6 mm·yr-1 and 0.3 mm·yr-1 of regional uplift rate **(d)** Schematic representation of main modeling results.

Supplementary Information

(Fault flexure and lithospheric rheology set from climate cycles in the Corinth Rift)

Gino de Gelder[1*], David Fernández-Blanco[1], Daniel Melnick[2,3], Guillaume Duclaux[4], Rebecca E. Bell[5], Julius Jara-Muñoz[2], Rolando Armijo[1] and Robin Lacassin[1])

This file includes 8 supplementary figures, and 2 supplementary table. Supplementary Figure 9 is a data repository and can be retrieved with this link:

https://figshare.com/s/bff68e81da9c540ae29f

Additionally, we share a georeferenced hillshade image and slope map of the 2 m-resolution Digital Surface Model that was developed from Pleiades satellite imagery, and formed the basis for marine terrace analysis. This image can be retrieved with these links:

https://figshare.com/s/05d6610458391e9da3d7(hillshade image)

https://figshare.com/s/a50519854408656e2532(slope map)

Supplementary text on numerical modelling

Supplementary Fig. 7 shows additional modelling results that serve to demonstrate that our main conclusions for 3-layer models are relatively insensitive to the chosen model set-up and parameters, whereas Supplementary Fig. 8 shows our 5-layer modelling results.

In Supplementary Fig. 7b we show with M11 that changing the recurrence time, while keeping the same slip rate, results in a visually indistinguishable deformation pattern. M12 shows that the effect of changing the slip rate can be well approximated by correcting the final displacement pattern, as is done in our tests to systematically find the slip rates and regional uplift rates with the lowest misfits to the data (Supplementary Fig. 7f, 8e). In Supplementary Fig. 7c we show that our choice of a model set-up with fixed sidewalls does not influence the final

deformation pattern significantly. M14 in Supplementary Fig. 7d shows that using two orders of magnitude lower viscosities with respect to M8 results in an unrealistic topographic evolution after >7 ka of running the model.

In Supplementary Figs. 7e and 7f we show that with a lower crustal viscosity of 1023, necessary to preserve the observed curvature of the elastic flexure signal, lower upper mantle viscosities than $5 \cdot 10^{21}$ Pa·s (M15) or higher viscosities than $2 \cdot 10^{22}$ Pa·s (M16, M17) result in too much and too little uplift respectively. Models with a 15km thick upper crust (Supplementary Fig. 7g) do not reproduce as much flexure of the curvature as M8 and M9 for the same upper crustal Young's Modulus and viscosity values (M18, M19), but with a strongly decreased upper crustal Young's Modulus (M20) we obtain good fits. This trade-off between upper crustal Young's Modulus and layer thickness has been proposed in several earlier studies (refs. 10,44 and references therein). Models with a lower fault angle (Supplementary Fig. 7h), require slightly lower upper mantle viscosities (M21, M22) with respect to M8 and M9 (Supplementary Fig. 7e) to obtain similarly good fits to the data.

The effects of introducing an elastoplastic upper crust instead of a purely elastic upper crust are presented in Supplementary Fig. 7i, and indicate that this does not change the uplift pattern much. Models with an elastoplastic upper crust and non-linear (powerlaw) viscoelastic lower crust (Supplementary Fig. 7j) produce a realistic surface deformation pattern on a ~30 ka timescale, but on the long term they produce an unrealistically low U:S ratio.

We also tested how to reproduce the same uplift pattern on a shorter timescale (2.4 ka instead of 240 ka; Supplementary Fig. 7l), and find that this requires ~100 times lower viscosities for the lower crust and upper mantle (M28-M30). Using the same high viscosities as M8 on a 2.4 ka timescale results in too little uplift (M31), whereas using the same low viscosities as M28 for a 240 ka timescale results in an unrealistic topographic evolution after ~7 ka (M14 in Supplementary Fig. 7d).

Our 5-layer models are presented in Supplementary Fig. 8. With a similar viscosity lower crust and upper mantle we find the lowest misfits for the models with basal lower crustal and basal upper mantle viscosities of $6 \cdot 10^{21}$ Pa·s (M34, M35 in Supplementary Fig. 8b,e Supplementary Table 2), whereas models with lower and higher viscosities produce too much (M32, M33) and too little uplift (M36, M37). For the models with a slightly higher viscosity lower crust than upper mantle (Supplementary Fig. 8c), we find low misfits for the models in which the difference between lower crust and upper mantle viscosity is relatively small (M42, M43 in Supplementary Fig. 8c,e Supplementary Table 2). Similarly, for the models with a slightly lower viscosity lower crust than upper mantle (Supplementary Fig. 8d), we also find low misfits for the models in which the difference between lower crust and upper mantle viscosity is relatively small (M46, M50 in Supplementary Fig. 8d,e Supplementary Table 2). Overall, this indicates that we require similar viscosities for lower crust and upper mantle to reproduce the deformation pattern with the 5-layer models.

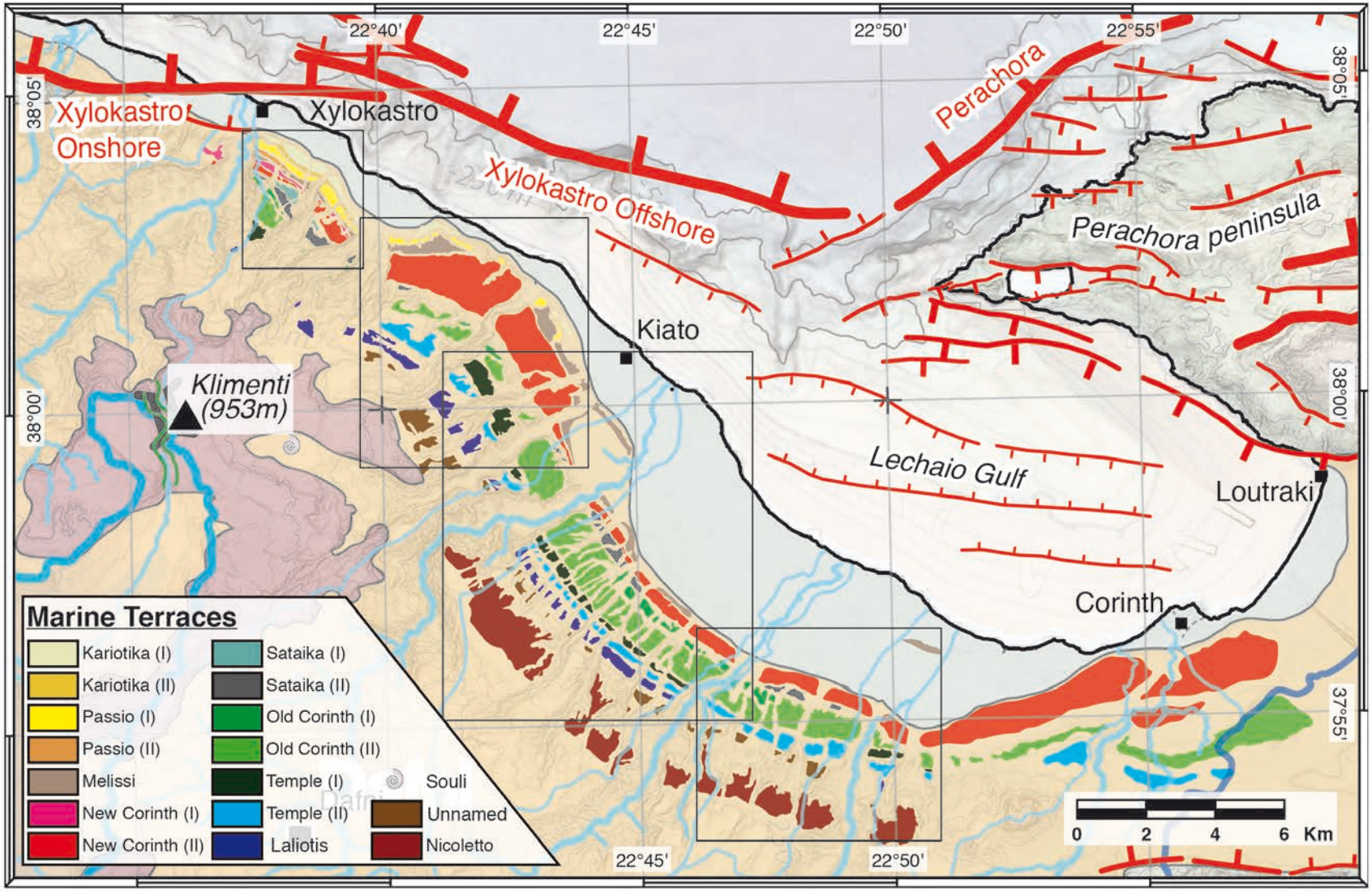
22°40'
22°45'
22°50'
22°55'
38°05'
38°00'
37°55'
Xylokastro Onshore
Xylokastro
Xylokastro Offshore
Perachora
Perachora peninsula
Kiato
Klimenti (953m)
Lechaio Gulf
Loutraki
Corinth
Marine Terraces
Kariotika (I)
Kariotika (II)
Passio (I)
Passio (II)
Melissi
New Corinth (I)
New Corinth (II)
Sataika (I)
Sataika (II)
Old Corinth (I)
Old Corinth (II)
Temple (I)
Temple (II)
Laliotis
Souli
Unnamed
Nicoletto
0 2 4 6 Km

Supplementary Figure 1 (previous page): **Marine terraces between Xylokastro and Corinth.** Based on detailed mapping with Pleiades DSM, with coloring and names modified from Armijo et al.[9]. Boxes indicate location of maps in Supplementary Fig. 8. Map was made using MAPublisher® version 9.8 (http://www.avenza.com/help/mapublisher/9.8/).

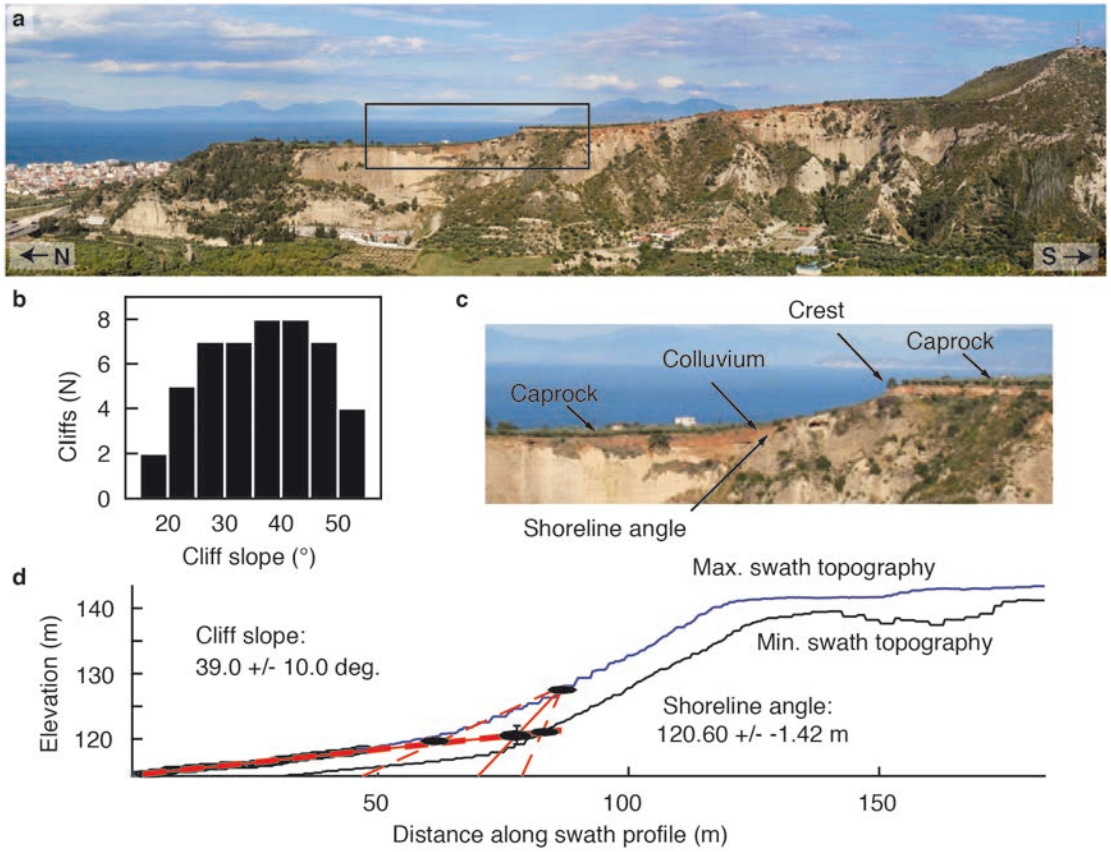

Supplementary Figure 2: Shoreline angle determination. (a) View of terraces near Xylokastro **(b)** Histogram of Holocene cliff slope measurements **(c)** Detail of terrace morphology from inset in **a (d)** Example of TerraceM shoreline angle analysis

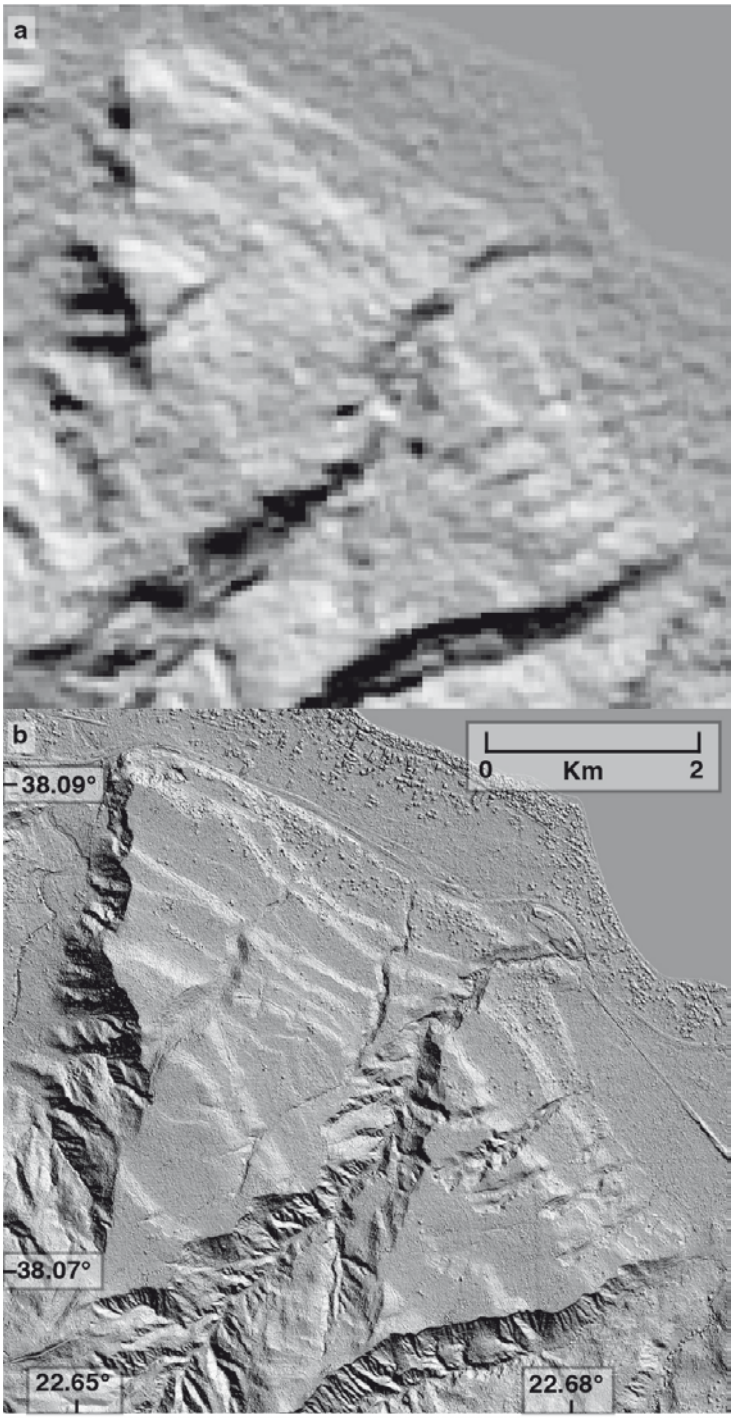

Supplementary Figure 3: Digital Elevation Model comparison. Hillshade images from **(a)** an ASTER DEM of 30m resolution and **(b)** a Pleiades DSM of 2m resolution.

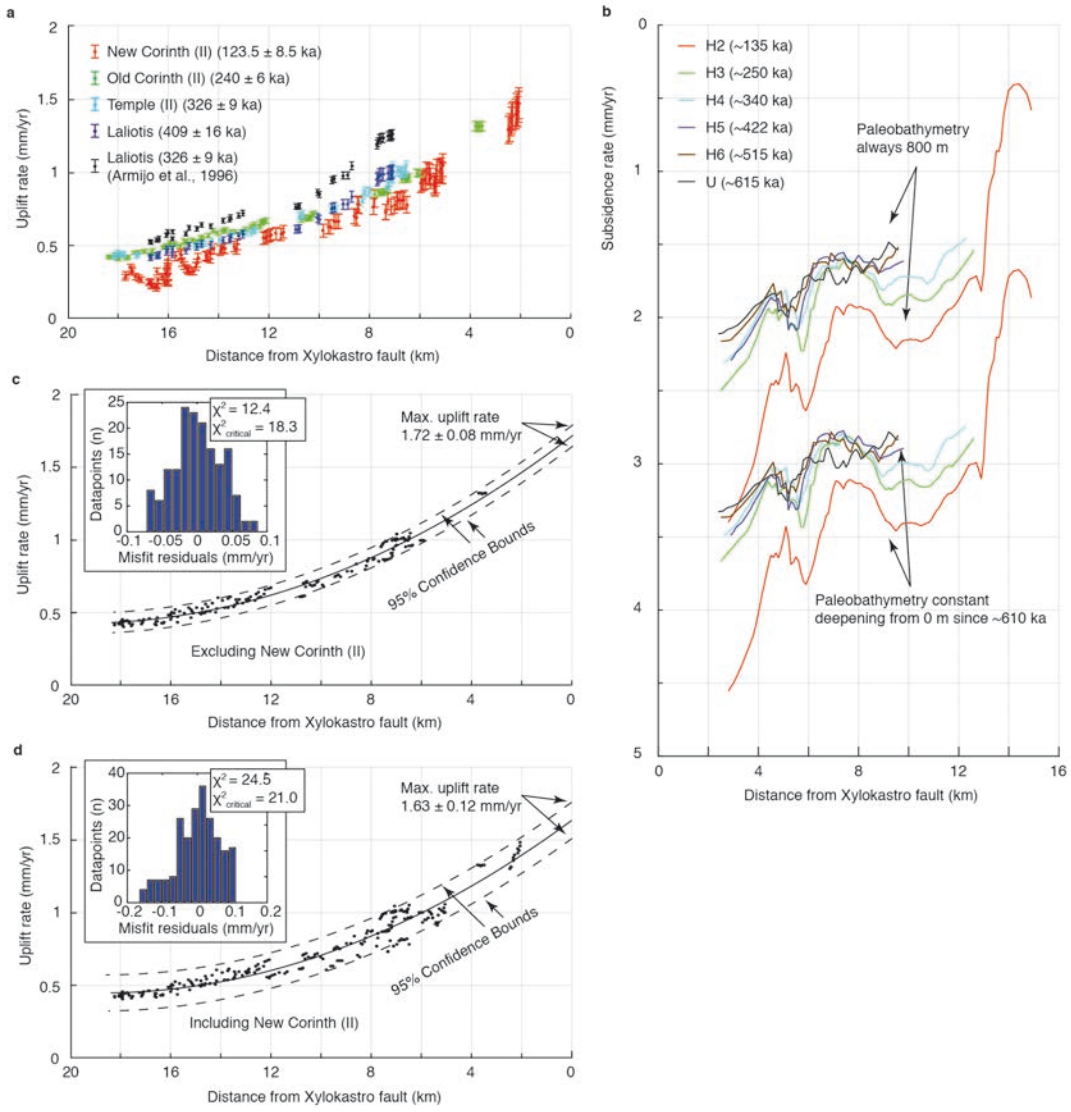

Supplementary Figure 4: Uplift/subsidence rates. (a) Estimated uplift rates for selected shoreline angles from Fig. 2f **(b)** Estimated subsidence rates for seismic horizons in Fig. 3 **(c)** Old Corinth (II), Temple (II) and Laliotis uplift rates grouped together and best fitting quadratic curve, including 95% confidence bounds, extrapolated to estimate uplift rate near fault. Inset shows histogram of residuals and values for critical χ^2 test. **(d)** Same as **c**, but including the New Corinth (II) terrace

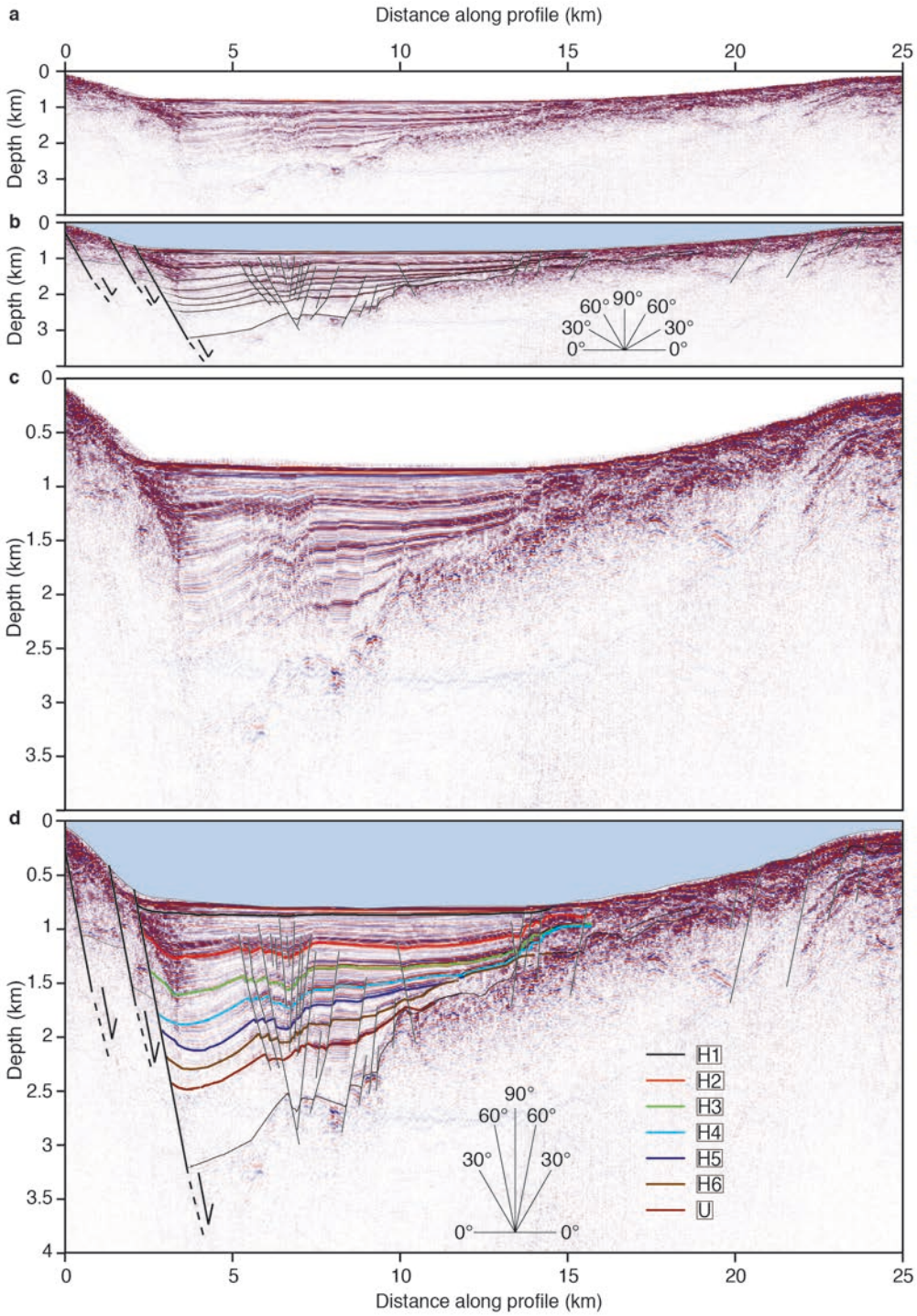

Supplementary Figure 5: Converted offshore seismic section of line L35[13]**. (a)** Without interpretation and vertical exaggeration **(b)** With interpretation from Nixon et al.[34] and without vertical exaggeration **(c)** Without interpretation and with 3x vertical exaggeration **(d)** With interpretation from Nixon et al.[34] and 3x vertical exaggeration.

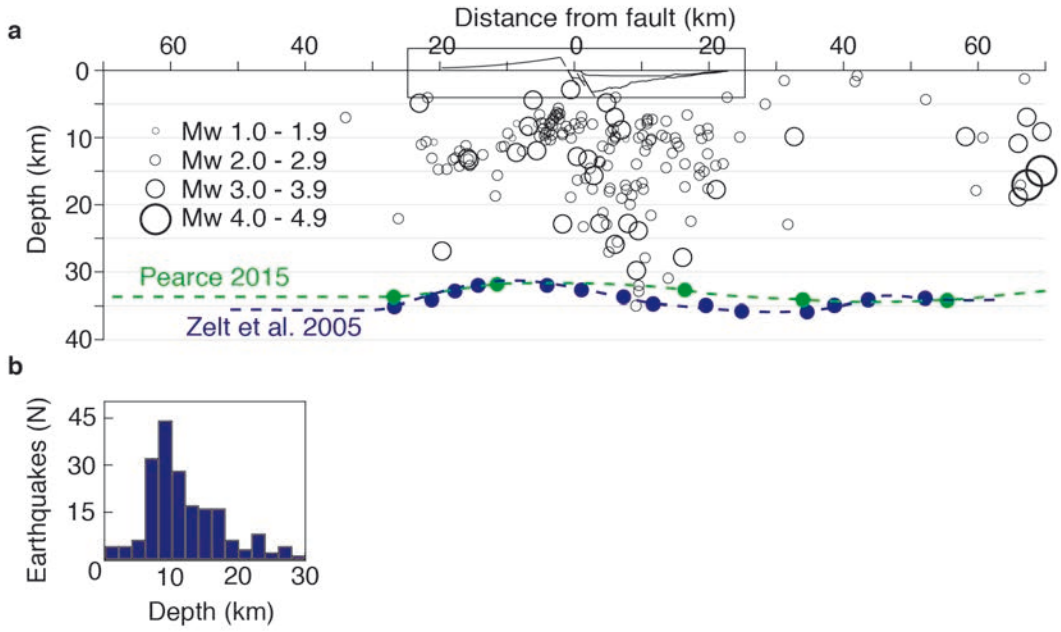

Supplementary Figure 6: Crustal scale cross-section. (a) Microseismicity from the University of Athens 1996-2008 earthquake catalogue measured within 2.5 km of profile A-A' in Fig. 1 and Moho depth estimates from Ps receiver functions[67] and tomographic inversion of PmP reflection times[68] **(b)** Histogram of (micro-)earthquake depths.

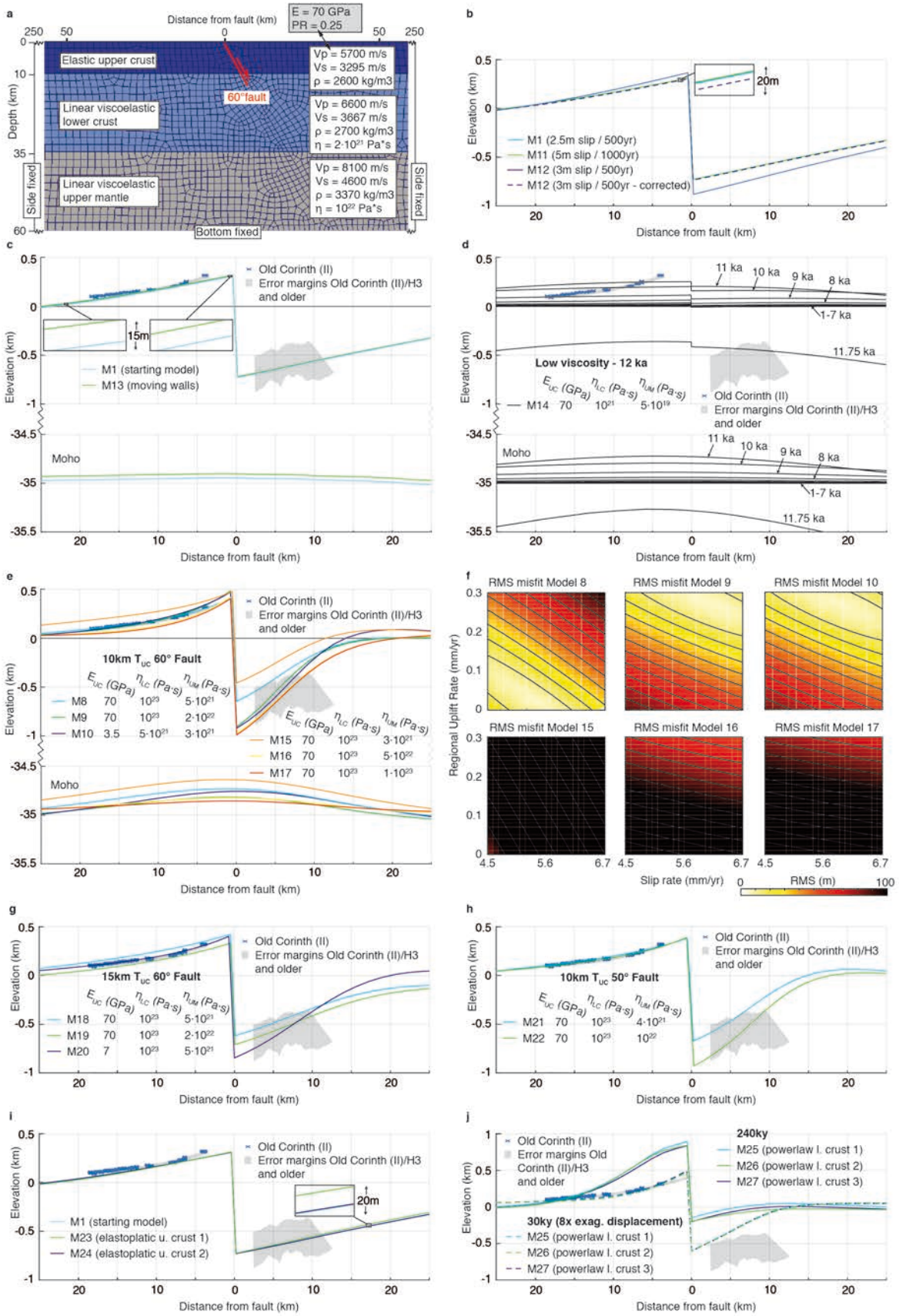
a
Distance from fault (km)
E = 70 GPa
PR = 0.25
Elastic upper crust
Vp = 5700 m/s
Vs = 3295 m/s
ρ = 2600 kg/m3
60°fault
Linear viscoelastic lower crust
Vp = 6600 m/s
Vs = 3667 m/s
ρ = 2700 kg/m3
η = 2·10^21 Pa*s
Linear viscoelastic upper mantle
Vp = 8100 m/s
Vs = 4600 m/s
ρ = 3370 kg/m3
η = 10^22 Pa*s
Side fixed
Bottom fixed
Depth (km)
b
20m
M1 (2.5m slip / 500yr)
M11 (5m slip / 1000yr)
M12 (3m slip / 500yr)
M12 (3m slip / 500yr - corrected)
Elevation (km)
Distance from fault (km)
c
Old Corinth (II)
Error margins Old Corinth (II)/H3 and older
15m
M1 (starting model)
M13 (moving walls)
Moho
d
11 ka
10 ka
9 ka
8 ka
1-7 ka
11.75 ka
Low viscosity - 12 ka
E_UC (GPa) η_LC (Pa·s) η_UM (Pa·s)
M14 70 10^21 5·10^19
e
10km T_UC 60° Fault
E_UC (GPa) η_LC (Pa·s) η_UM (Pa·s)
M8 70 10^23 5·10^21
M9 70 10^23 2·10^22
M10 3.5 5·10^21 3·10^21
M15 70 10^23 3·10^21
M16 70 10^23 5·10^22
M17 70 10^23 1·10^23
f
RMS misfit Model 8
RMS misfit Model 9
RMS misfit Model 10
RMS misfit Model 15
RMS misfit Model 16
RMS misfit Model 17
Regional Uplift Rate (mm/yr)
Slip rate (mm/yr)
RMS (m)
g
15km T_UC 60° Fault
M18 70 10^23 5·10^21
M19 70 10^23 2·10^22
M20 7 10^23 5·10^21
h
10km T_UC 50° Fault
M21 70 10^23 4·10^21
M22 70 10^23 10^22
i
M1 (starting model)
M23 (elastoplatic u. crust 1)
M24 (elastoplatic u. crust 2)
j
240ky
M25 (powerlaw l. crust 1)
M26 (powerlaw l. crust 2)
M27 (powerlaw l. crust 3)
30ky (8x exag. displacement)

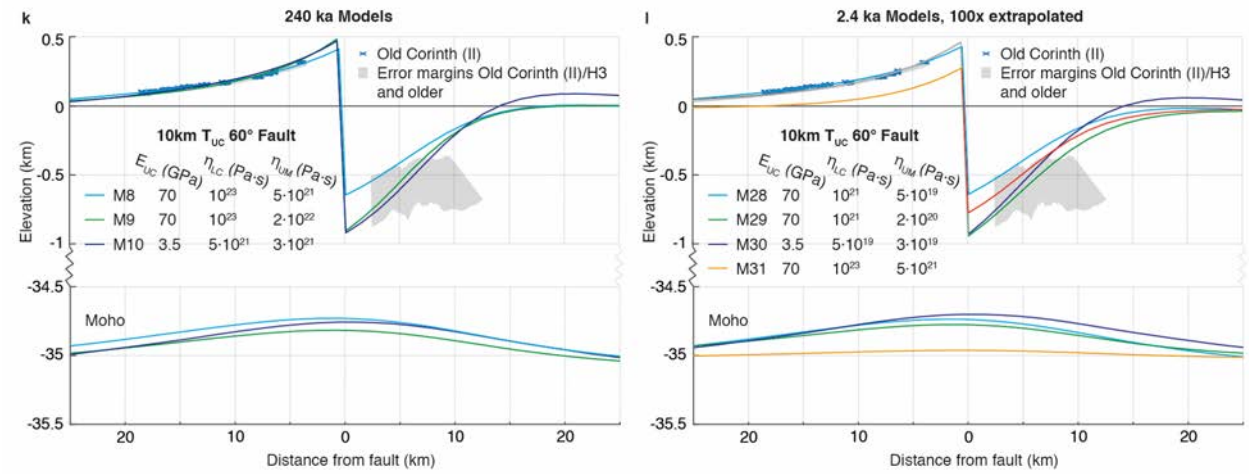

Supplementary Figure 7 (including previous page): Additional fault modelling results. (a) Subset of finite element grid showing Model 1 set-up. E = Young's Modulus, PR = Poisson's Ratio, Vp = P-wave velocity, Vs = S-wave velocity, ρ = density, η = viscosity **(b)** Tests on the influence of different earthquake recurrence time (M11) and slip rate (M12), the latter both uncorrected and with total displacement corrected by a factor 0.83 **(c)** Model with the same parameters as Model 1, but with 0.125 $mm \cdot yr^{-1}$ laterally moving sidewalls, and bottomwall moving upwards with 0.03 $mm \cdot yr^{-1}$ to isostatically compensate for lithospheric thinning **(d)** Example of model with two orders of magnitude lower viscosities with respect to M8, with timesteps plotted for every 1000 years until the model stops running after ~12 ka **(e)** Models 8-10 from Fig. 5b for comparison with g-l, including models with too low (M15) and too high (M16, M17) upper mantle viscosities for comparison **(f)** Root-mean-squared misfits of models 8-10 and 15-17 under the assumption of different fault slip rates and regional uplift rates. **(g)** Models with a 15km thick upper crust and 60° fault **(h)** Models with a 10 km thick upper crust and 50° fault **(i)** Models with an elastoplastic upper crust compared to Model 1 **(j)** Models with an elastoplastic upper crust and non-linear (powerlaw) viscoelastic lower crust compared to Model 1. **(k)** Repetition of Fig. 5c for comparison **(l)** Model results for viscosity values two orders of magnitude lower than M8-10 (M28-30) and the same as M8 (M31), but on a 2.4 ka timescale, plotted with a 100 times extrapolation of the surface deformation pattern.

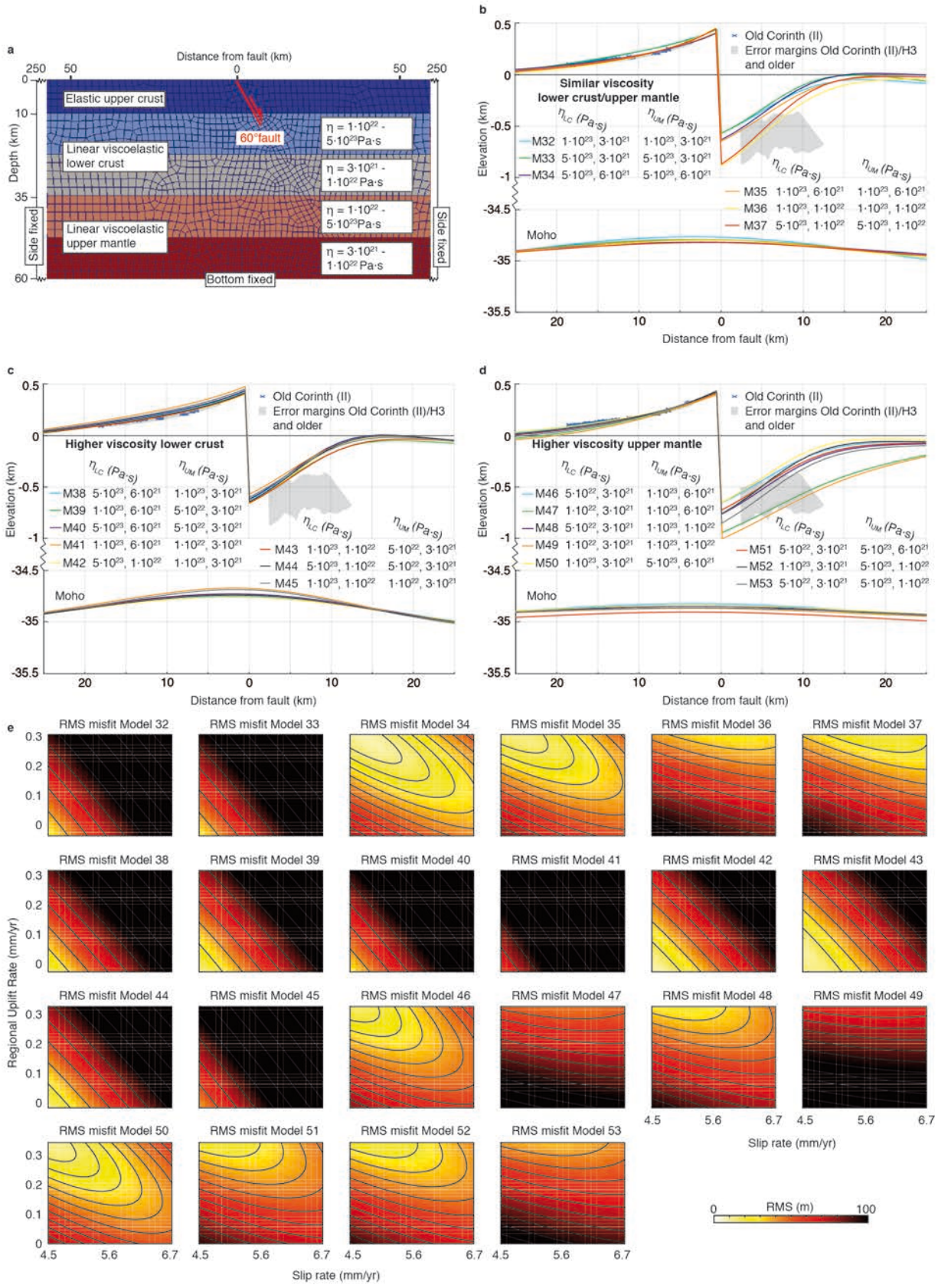
a
Distance from fault (km)
Elastic upper crust
60°fault
Linear viscoelastic lower crust
Linear viscoelastic upper mantle
Side fixed
Bottom fixed
Depth (km)
b
Old Corinth (II)
Error margins Old Corinth (II)/H3 and older
Similar viscosity lower crust/upper mantle
Moho
Elevation (km)
Distance from fault (km)
c
Higher viscosity lower crust
d
Higher viscosity upper mantle
e
RMS misfit Model 32
RMS misfit Model 33
RMS misfit Model 34
RMS misfit Model 35
RMS misfit Model 36
RMS misfit Model 37
RMS misfit Model 38
RMS misfit Model 39
RMS misfit Model 40
RMS misfit Model 41
RMS misfit Model 42
RMS misfit Model 43
RMS misfit Model 44
RMS misfit Model 45
RMS misfit Model 46
RMS misfit Model 47
RMS misfit Model 48
RMS misfit Model 49
RMS misfit Model 50
RMS misfit Model 51
RMS misfit Model 52
RMS misfit Model 53
Regional Uplift Rate (mm/yr)
Slip rate (mm/yr)
RMS (m)

Supplementary Figure 8 (previous page): Additional fault modelling for 5-layer models (a) Subset of finite element grid showing 5-layer model set-up. Fault angle, Upper crustal Young's Modulus and upper crustal thickness are the same as in M1 **(b-d)** Results for models with the same (**b**), higher (**c**) and lower (**d**) lower crustal viscosity with respect to the upper mantle. All models are plotted with the regional uplift rates and slip rates that correspond to their minimum root-mean-squared misfit (see **e** and Supplementary Table 2) **(e)** Root-mean-squared misfits of models 32-53 under the assumption of different fault slip rates and regional uplift rates.

Table S1. Input parameters for numerical fault models

Elastic upper crust – linear viscoelastic lower crust – linear viscoelastic upper mantle

Model Nr.	Young's Modulus U.Crust (GPa)	Upper Crustal Thickness (km)	Fault Angle (°)	L. Crustal Viscosity (Pa·s)	U. Mantle Viscosity (Pa·s)
1	70	10	60	$2 \cdot 10^{21}$	10^{22}
2	7	10	60	$2 \cdot 10^{21}$	10^{22}
3	70	15	60	$2 \cdot 10^{21}$	10^{22}
4	70	10	40	$2 \cdot 10^{21}$	10^{22}
5	70	10	60	10^{22}	10^{22}
6	70	10	60	$2 \cdot 10^{21}$	10^{23}
7*	70	10	60	$2 \cdot 10^{21}$	10^{22}
8	70	10	60	10^{23}	$5 \cdot 10^{21}$
9	70	10	60	10^{23}	$2 \cdot 10^{22}$
10	3.5	10	60	$5 \cdot 10^{21}$	$3 \cdot 10^{21}$
11**	70	10	60	$2 \cdot 10^{21}$	10^{22}
12***	70	10	60	$2 \cdot 10^{21}$	10^{22}
13****	70	10	60	$2 \cdot 10^{21}$	10^{22}
14	70	10	60	10^{21}	$5 \cdot 10^{19}$
15	70	10	60	10^{23}	$3 \cdot 10^{21}$
16	70	10	60	10^{23}	$5 \cdot 10^{22}$
17	70	10	60	10^{23}	10^{23}
18	70	15	60	10^{23}	$5 \cdot 10^{21}$
19	70	15	60	10^{23}	$2 \cdot 10^{22}$
20	7	15	60	10^{23}	$5 \cdot 10^{21}$
21	70	10	50	10^{23}	$4 \cdot 10^{21}$
22	70	10	50	10^{23}	$8 \cdot 10^{21}$

* Same parameters as model 1, but with a fault crosscutting the whole crust at a 60° angle
** Same parameters as model 1, but with 5m slip earthquakes every 1000 years instead of 2.5m slip earthquakes every 500 years
*** Same parameters as model 1, but with 3m slip earthquakes every 500 years instead of 2.5m slip earthquakes every 500 years
**** Same parameters as model 1, but with walls laterally moving 0.125 mm/yr at both sides of the model, and upwards with 0.03 mm/yr at the bottom of the model

Elastoplastic upper crust – linear viscoelastic lower crust – linear viscoelastic upper mantle

Model Nr.	Cohesion (MPa)	Internal friction angle (°)	Dilatation angle (°)
23*	10	20	20
24*	50	30	30

* All other parameters same as model 1

Elastoplastic upper crust – non-linear (powerlaw) viscoelastic lower crust – linear viscoelastic upper mantle

Model Nr.	Temperature lower crust (°C)	Powerlaw stress exponent	Activation energy Q ($kJ \cdot mol^{-1}$)	Pre-exponential term A ($MPa^{-n} \cdot s^{-1}$)	U. Mantle Viscosity (Pa·s)
25*	300-720	4.0	223	$1.1 \cdot 10^{-4}$	10^{22}
26*	300-650	4.0	223	$1.1 \cdot 10^{-4}$	10^{22}
27*	300-720	4.0	223	$1.1 \cdot 10^{-4}$	10^{23}

* All other parameters same as model 18

Table S2. Viscosities and misfits for numerical fault models

3-Layer models with 10 km crustal thickness, 60° fault angle, and 70 GPa Upper Crustal Young's Modulus

Model Nr.	L. Crustal Viscosity 10 – 35 km (Pa·s)	U. Mantle Viscosity 35 – 60 km (Pa·s)	Plotted slip rate ($mm \cdot yr^{-1}$)	Plotted regional uplift rate ($mm \cdot yr^{-1}$)	RMS misfit (m)
15	$1 \cdot 10^{23}$	$3 \cdot 10^{21}$	4.5	0.0	85.7
8	$1 \cdot 10^{23}$	$5 \cdot 10^{21}$	5.1	0.01	7.4
9	$1 \cdot 10^{23}$	$2 \cdot 10^{22}$	5.5	0.27	7.1
16	$1 \cdot 10^{23}$	$5 \cdot 10^{22}$	6.7	0.3	52.2
17	$1 \cdot 10^{23}$	$1 \cdot 10^{23}$	6.7	0.3	63.9

5-Layer models with 10 km crustal thickness, 60° fault angle, and 70 GPa Upper Crustal Young's Modulus

Model Nr.	L. Crustal Viscosity 10 – 22.5 km (Pa·s)	L. Crustal Viscosity 22.5 – 35 km(Pa·s)	U. Mantle Viscosity 35 – 47.5 km (Pa·s)	U. Mantle Viscosity 47.5 – 60 km (Pa·s)	Plotted slip rate ($mm \cdot yr^{-1}$)	Plotted regional uplift rate ($mm \cdot yr^{-1}$)	RMS misfit (m)
32	$1 \cdot 10^{23}$	$3 \cdot 10^{21}$	$1 \cdot 10^{23}$	$3 \cdot 10^{21}$	4.5	0.0	27.4
33	$5 \cdot 10^{23}$	$3 \cdot 10^{21}$	$5 \cdot 10^{23}$	$3 \cdot 10^{21}$	4.5	0.0	28.7
34	$5 \cdot 10^{23}$	$6 \cdot 10^{21}$	$5 \cdot 10^{23}$	$6 \cdot 10^{21}$	4.6	0.3	8.4
35	$1 \cdot 10^{23}$	$6 \cdot 10^{21}$	$1 \cdot 10^{23}$	$6 \cdot 10^{21}$	4.7	0.3	11.4
36	$1 \cdot 10^{23}$	$1 \cdot 10^{22}$	$1 \cdot 10^{23}$	$1 \cdot 10^{22}$	5.9	0.3	25.8
37	$5 \cdot 10^{23}$	$1 \cdot 10^{22}$	$5 \cdot 10^{23}$	$1 \cdot 10^{22}$	5.8	0.3	16.7
38	$5 \cdot 10^{23}$	$6 \cdot 10^{21}$	$1 \cdot 10^{23}$	$3 \cdot 10^{21}$	4.5	0.0	19.3
39	$1 \cdot 10^{23}$	$6 \cdot 10^{21}$	$5 \cdot 10^{22}$	$3 \cdot 10^{21}$	4.5	0.0	14.9
40	$5 \cdot 10^{23}$	$6 \cdot 10^{21}$	$5 \cdot 10^{22}$	$3 \cdot 10^{21}$	4.5	0.0	29.2
41	$1 \cdot 10^{23}$	$6 \cdot 10^{21}$	$1 \cdot 10^{22}$	$3 \cdot 10^{21}$	4.5	0.0	60.1
42	$5 \cdot 10^{23}$	$1 \cdot 10^{22}$	$1 \cdot 10^{23}$	$3 \cdot 10^{21}$	4.5	0.0	9.5
43	$1 \cdot 10^{23}$	$1 \cdot 10^{22}$	$5 \cdot 10^{22}$	$3 \cdot 10^{21}$	4.5	0.04	10.8
44	$5 \cdot 10^{23}$	$1 \cdot 10^{22}$	$5 \cdot 10^{22}$	$3 \cdot 10^{21}$	4.5	0.0	14.0
45	$1 \cdot 10^{23}$	$1 \cdot 10^{22}$	$1 \cdot 10^{22}$	$3 \cdot 10^{21}$	4.5	0.0	40.9
46	$5 \cdot 10^{22}$	$3 \cdot 10^{21}$	$1 \cdot 10^{23}$	$6 \cdot 10^{21}$	4.5	0.3	14.8
47	$1 \cdot 10^{22}$	$3 \cdot 10^{21}$	$1 \cdot 10^{23}$	$6 \cdot 10^{21}$	5.6	0.3	43.8
48	$5 \cdot 10^{22}$	$3 \cdot 10^{21}$	$1 \cdot 10^{23}$	$1 \cdot 10^{22}$	5.0	0.3	24.7
49	$1 \cdot 10^{22}$	$3 \cdot 10^{21}$	$1 \cdot 10^{23}$	$1 \cdot 10^{22}$	5.8	0.3	58.0
50	$1 \cdot 10^{23}$	$3 \cdot 10^{21}$	$5 \cdot 10^{23}$	$6 \cdot 10^{21}$	4.5	0.3	11.4
51	$5 \cdot 10^{22}$	$3 \cdot 10^{21}$	$5 \cdot 10^{23}$	$6 \cdot 10^{21}$	4.8	0.3	21.4
52	$1 \cdot 10^{23}$	$3 \cdot 10^{21}$	$5 \cdot 10^{23}$	$1 \cdot 10^{22}$	5.0	0.3	19.1
53	$5 \cdot 10^{22}$	$3 \cdot 10^{21}$	$5 \cdot 10^{23}$	$1 \cdot 10^{22}$	5.4	0.3	33.6